Improved Bandwidth Carbon Fiber Reinforced Plastic Structural Antenna Design for near-HF Remote Sensing Applications

By

Andrew Rios
B.S., University of Texas at El Paso, 2020

Submitted to the graduate degree program in Aerospace Engineering and the Graduate Faculty of the University of Kansas in partial fulfillment of the requirements for the degree of Master of Science.

Chair: Dr. Emily Arnold

Dr. Richard Hale

Dr. Mark Ewing

Date Defended: 9 May 2022

The thesis committee for Andrew Rios certifies that this is the approved version of the following thesis:

Improved Bandwidth Carbon Fiber Reinforced Plastic Structural Antenna Design for near-HF Remote Sensing Applications

Chair: Dr. Emily Arnold

Date Approved: 9 May 2022

Abstract

This work presents an improved bandwidth antenna design for the HF Sounder radar installed on a Twin Otter. This is achieved by replacing the original steel tube dipole antenna with a larger and more aerodynamic carbon fiber reinforced plastic (CFRP) antenna. CFRP is a sufficiently conductive material and its density is about 20% the density of 4130-steel, so by replacing the original steel design with a CFRP design, a larger antenna can be supported, resulting in an expected wider operational bandwidth. Initially several aerodynamic cross-sections are considered for the larger antenna, and a trade study is performed to compare the various designs to the original tube design. This trade study considers electrical performance (specifically bandwidth), implications to aircraft range, and assessment of the structural design. From the initial trade study, two aerodynamic shapes are considered for further assessment—an ellipse with a t/c ratio of 0.33 and a NACA 0024 airfoil. Based on this study, a 2 in. x 8 in. NACA 0024 antenna is manufactured and physically tested. Experimental electrical testing has verified that the newly developed CFRP antenna works as simulated and has 1.7 times improved bandwidth compared to the tube antenna. The airfoil antenna design is expected to improve the bandwidth, is expected to improve the vehicle range, and initial sizing suggests that the structural concept is feasible.

Acknowledgements

I would like to thank Dr. Arnold for her continuous support in my studies and research. I want to express my appreciation for all the time she put in to help me succeed. I also want to thank my committee members for their comments and suggestions that helped me improve my research. Thank you to my mom for supporting me all the way up to this moment in my life. She has always put her children first and I would not be here without her. I know my dad would have been proud to see me get to this point as well. Thank you to my brother and sister for their support and always being there for me. Thank you to my girlfriend, Bianca, for supporting me. Having her here with me during my time at KU has meant so much and made my experience that much better.

Table of Contents

Nomenclature

Symbol	Description	Units
AR	Aspect ratio	~
C	Carbon fiber biaxial cloth	~
c_d	2D total drag coefficient	~
c_{d_o}	2D drag coefficient at zero lift	~
c_l	2D coefficient of lift	~
D	Drag force	lbs.
E	Modulus of elasticity	ksi
G	Shear modulus	ksi
I	Second moment of area	in^4
L	Lift force	lbs.
l	Antenna arm length	in.
M	Moment	lb.-in.
r	Radius	in.
S_{11}	S-parameter	dB
S	Planform area	in^2
St	4130-steel	~
t/c	Thickness-to-chord ratio	~
V	Velocity	ft/s

Greek	Description	Units
σ	Bending stress	ksi
τ	Shear stress	ksi
ρ	Density	lb_m/ft^3
ν	Poisson's ratio	~

Subscripts	Description
actual	Applied load or stress
allowable	Allowable strength or stress
c	Compressive
mc	Minimum control
ne	Never exceed
t	Tensile
u	Ultimate
y	Yield
1	Primary material axis
2	Secondary material axis
12	Shear axis

List of Figures

List of Tables

1. Introduction

Airborne radar remote sensing has become an indispensable tool in many geoscience fields for conducting earth observations. Airborne platforms allow for much broader spatial coverage as compared to *in situ* measurements and higher spatial resolution as compared to satellite-based measurements. The Center for Remote Sensing of Ice Sheets (CReSIS) at the University of Kansas has developed an airborne temperate ice sounding radar known as the "HF Sounder" [1]. The dual-frequency radar system has two operating modes. One operating mode is centered around 14 MHz (Mode 1) and the other is centered around 30 MHz (Mode 2). The latter mode has been the primary operating mode of the system. This near-high frequency (near-HF) system has been flown on both a Twin Otter and a small Unmanned Aerial System (UAS) that has a maximum takeoff weight of 75 lbs. and a 9.9 ft wing span [1]. The antenna installation on the Twin Otter can be seen in Figure 1. While both of these systems have successfully sounded and detected the ice bottom of several temperate glaciers in Greenland, the performance of both systems was limited by the antenna. One of the primary technical challenges related to developing new airborne radar systems is the integration of the antenna, particularly for operating frequencies in the Very High Frequency (VHF) spectrum and lower. Because antenna size is inversely proportional to the operating frequency, antennas in these frequency ranges tend to be very large, thus requiring integration external to the airframe. Further complicating integration of such antennas is the conductive nature of the airframe, which couples and interferes with the antenna performance.

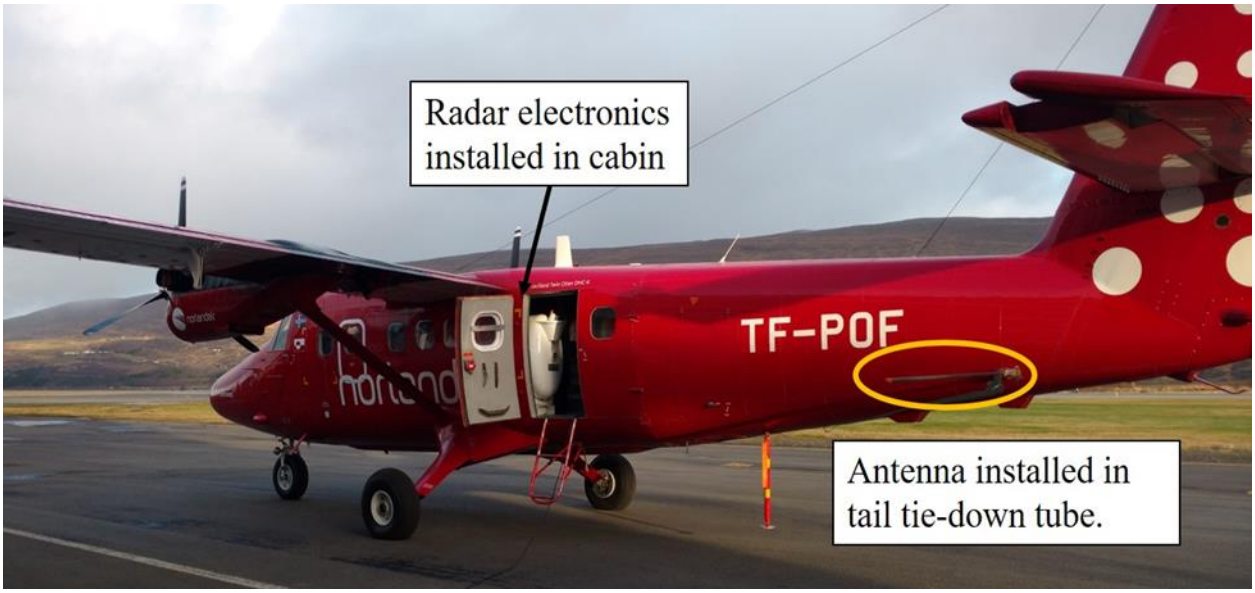

Figure 1: Original Dipole Antenna Installation on Twin Otter

The goal of the HF Sounder design was to improve radar sensing of temperate ice regions. It was developed to replace VHF radars that have not had reliable operation in these regions. The Twin Otter HF Sounder antenna consisted of a single steel dipole element. It was tested over the Hofsjökull ice cap in Iceland and then flown over Greenland as part of a 2016 field deployment over the primary target of the Jakobshavn glacier, Greenland. The results of the 2016 mission showed improvement over using VHF radars in these regions with reduced scatter and improved ice bottom detection [1]. The study presented in this paper looked into antenna concepts that might provide improved bandwidth while maintaining comparable drag. Improving the bandwidth of the antenna would result in better data acquisition for future missions. There is also a desire to develop a multi-channel (antenna element) system for the Twin Otter where an element would be mounted on each wing in addition to the element within the tail. The antenna within the tail section is the main design focus of this paper, but this future configuration was kept in mind during the design to ensure that drag was minimized to maintain vehicle range and mission viability.

Recently, the conductivity of carbon fiber reinforced plastic (CFRP) materials was characterized for structural antenna applications and it was found that CFRP antennas can perform comparably to equivalent copper antennas in the VHF and lower spectra [2]. Generally, the conducting elements of antennas are made of copper or aluminum due to their superior conductivity, but the density of these materials are between 50%-500% higher than CFRP. It is well known that the bandwidth of an antenna is directly related to the size of the antenna. In an effort to try to improve the bandwidth for future missions, an antenna with a larger cross-section is desired. CFRP is a sufficiently conductive material and its density is about 20% the density of 4130-steel, so by replacing the original steel design with a CFRP design, a larger antenna can be supported, resulting in a wider operational bandwidth. This paper discusses the design of an improved bandwidth antenna. First, an overview is provided of the original antenna installed in the tail tie-down tube of the Twin Otter. Then an initial trade study is introduced that assesses electrical performance, drag effects on vehicle range, and structural stability of six candidate designs. A comparison is presented of the original tube and two well performing candidate designs, as well as a structural analysis of a final structural design. Experimental electrical testing is performed on a prototype design and discussed. Lastly, the conclusions of the paper are provided, including recommendations for future work.

2. Original Twin Otter Dipole Antenna

2.1 Design Overview and Restrictions

The high-powered version of the HF Sounder was first flown on Norlandair's Twin Otter aircraft as part of a 2016 field deployment over Jakobshavn glacier, Greenland [1]. For the antenna integration, a major design driver was the restriction that the airframe of the Twin Otter could not be modified to avoid costly certification approvals. This restricted the viable vehicle integration locations to a tail tie-down tube, and the lack of mounting supports on the aircraft thus limited the antenna sizing and tuning. The original antenna for the HF Sounder was designed as a single dipole element with the two dipole arms connected at the middle inside the tie-down tube. An overview of the antenna assembly and installation on the Twin Otter is shown in Figure 2. The portion between the polycarbonate cuffs is interior to the aircraft and in the tail tie-down tube. Only the cuffs, metal sleeves, and dipole arm are exposed to the freestream air. The dipole antenna is a 4130-steel tube with an outer diameter of 1.25 in. and a thickness of 0.125 in. The total dipole length is 192 in. The length of one arm is 96 in. with 6.5 in. inside the tail tube and 89.5 in. outside the mold line of the aircraft.

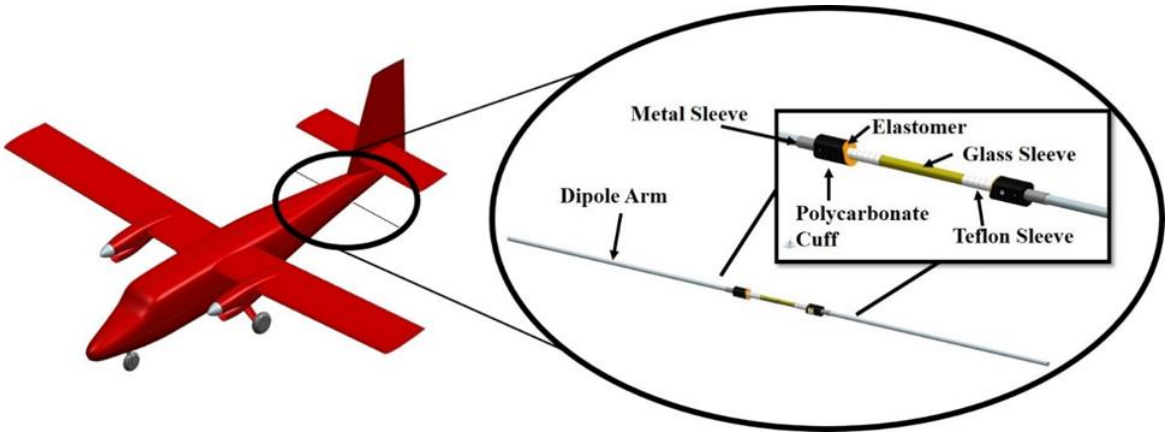

Figure 2: Overview of Original Dipole Assembly

The original antenna was sized to the aircraft maximum dynamic pressure of 0.77 psi (never exceed velocity of 287 ft/s) and the analysis assumed a drag coefficient for a circular 2D cross-section of 1.13 from Ref. [3]. In addition, to avoid any adverse mechanical coupling, it was necessary to design the vibration modes (natural frequencies) to be outside of the blade passage frequency of the vehicle. The Twin Otter has a maximum propeller speed of 2,200 rpm and has three blades on its turboprop engines. This results in a blade passage frequency of 110 Hz. The first five natural frequencies for the original antenna were calculated to be 5.6 Hz, 35.2 Hz, 98.4 Hz, 192.8 Hz, and 318.8 Hz.

2.2 Antenna Performance

The original antenna was simulated to determine the electrical performance using Ansys High Frequency Structure Simulator (HFSS) software [4] and was tuned to have a center frequency around 30 MHz (with the idea that the 14 MHz mode (Mode 1) frequency range could be achieved by integrating an impedance matching network). The installed Twin Otter HF Sounder was tested over the Hofsjökull ice cap in Iceland prior to the transit over Greenland. The installed antenna used a two lumped-element impedance Matching Network (MN) for dual frequency operation and improved impedance bandwidth across the 30 MHz (Mode 2) band. Figure 3 shows the S_{11} of the simulated antenna (dashed red) as well as the measured S_{11} of the installed antenna on the Twin Otter, both with (blue) and without (red) the Mode 2 matching network. In the simulation, the antenna had a resonant frequency of 30.4 MHz and a 10-dB impedance bandwidth of 1.5 MHz (29.6 MHz – 31.1 MHz), while the installed antenna had a measured resonance frequency of 30.8 MHz and a bandwidth of 4.5 MHz. The change in S_{11} for the installed antenna is attributed to coupling of the antenna with the aircraft. With the addition of the MN, the 10-dB impedance

bandwidth only improved to 5 MHz due to the slight bump in the response at 28 MHz. During simulation, the MN was predicted to improve the bandwidth to 9 MHz (25.5 MHz-34.5 MHz). The imperfect response is again attributed to the aircraft integration affects (such as coupling with the vehicle) that are difficult to characterize in simulations and ground measurements.

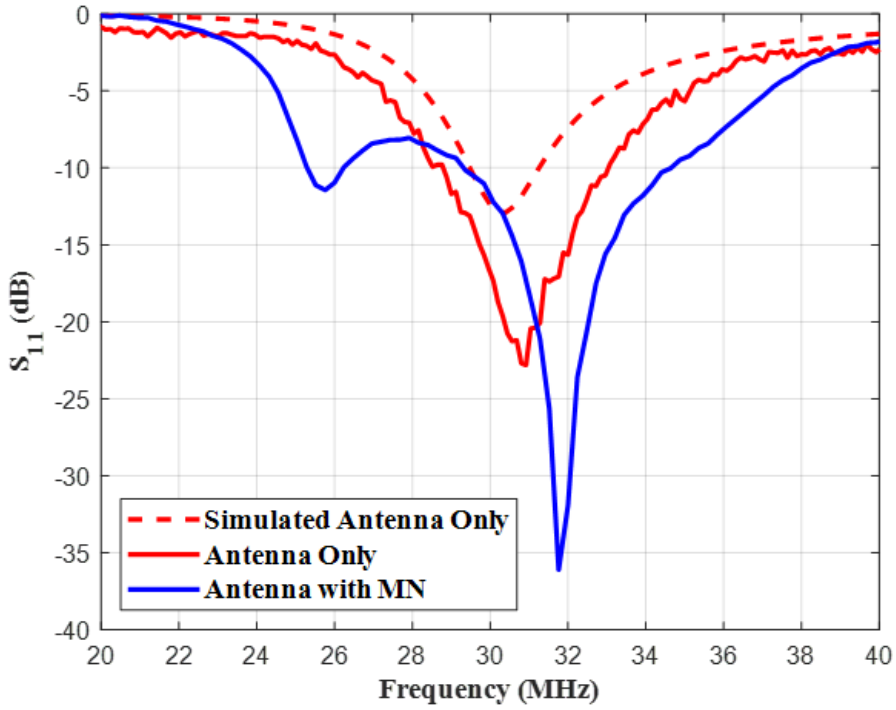

Figure 3: Comparison of Simulated and In-flight S_{11} of Original Antenna Installed on the Twin Otter

A larger antenna design is desired to increase operational bandwidth. However, the overall size of the antenna was limited by the aerodynamic loads generated by the antenna and (more importantly) the fixed size of the tail tie-down tube. In addition, the drag of a larger antenna needs to be considered to mitigate vehicle range reduction, especially considering the potential future development of a multi-channel HF Sounder. Given the fixed bounding geometry, several new designs were considered that consisted of the original steel tube inserted through the tail tube that

then transitions to a larger cross-section fabricated from CFRP material. The following section summarizes the initial trade study conducted to determine candidate designs for the larger antenna. First, electrical performance is assessed for initial antenna sizing. Given that a gain measurement was never conducted with the original antenna, “electrical performance” will specifically focus on the resonance frequency and 10-dB impedance bandwidth. Next, the drag effects on vehicle range are considered. Then the a first-order stress analysis is conducted on six candidate designs to determine structural stability. A comparison is presented of the original tube and the two final candidate designs. Lastly, a more rigorous structural analysis is also performed on the final structural design.

3. Initial Trade Study

By transitioning from the metal tube to a CFRP section, larger and more aerodynamic sections could be considered. Figure 4 shows an overview of the general design that was considered for the larger antenna. It includes a CFRP skin, a tube for connection to the Twin Otter, and two ribs located at the inboard side of the CFRP skin. The tube and ribs are shown in blue and the skin is shown in grey. Designs were created using Siemens NX [5].

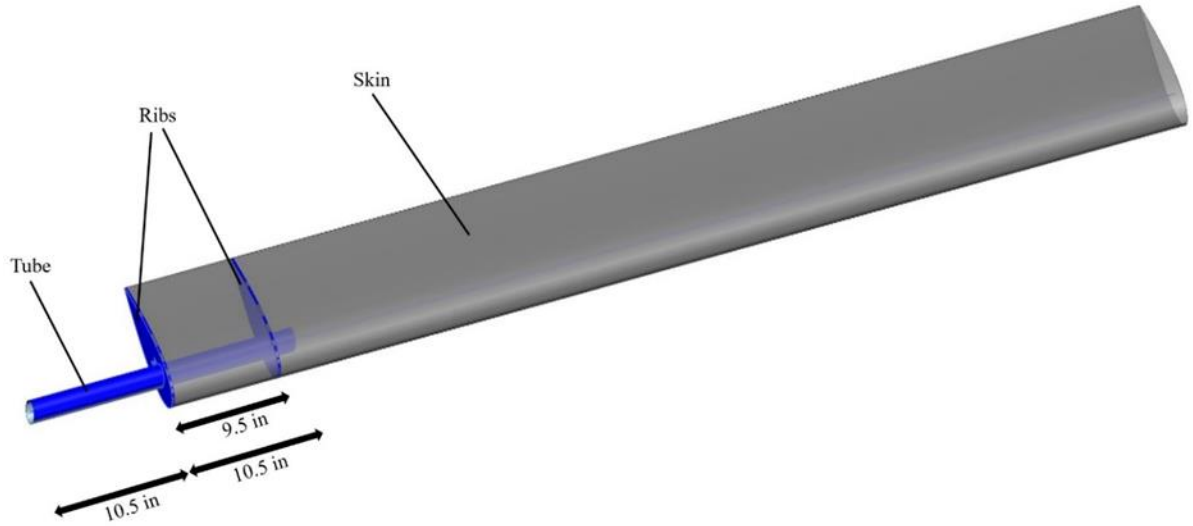

Figure 4: Single Arm of Larger Antenna Design

The large antenna size requirement was in direct conflict with the structural sizing of the antenna. Given the fixed size of the tail tie-down tube diameter, it was desirable to minimize the lift loads generated by the larger antenna planform. The effect of the antenna drag on the aircraft range was also an important factor that was considered in the design process. Vehicle range directly impacts the surveying mission, and too great of a reduction can make the vehicle nonviable. To compare the various designs, the electrical performance (specifically the 10-dB impedance

bandwidth) was first determined via simulation for a variety of aerodynamic cross-sections. Then a first-order structural analysis of the candidate designs along with their impacts on vehicle range were assessed to identify the recommended candidate design.

Only symmetric aerodynamic shapes were considered because they do not produce lift at zero angle of attack and it was necessary to minimize lift of the antenna to minimize the flexural stress while in flight. These shapes included several ellipses and airfoils with large thickness-to-chord ratios to maximize the potential cross-section size that could be achieved (which is beneficial for electrical performance). The design variables included the antenna length, t/c for the airfoils, and the major and minor axes of the ellipses. Parametric electromagnetic simulations were used to determine the effects of changing these dimensions to maximize the bandwidth of the antenna.

3.1 Size vs. Electrical Performance

The electrical performance of the new antenna designs was simulated using Ansys HFSS software [4]. A parametric analysis was performed for several elliptical antennas and all designs were tuned to resonate at 30 MHz by varying dipole arm lengths, ellipse major axis, and ellipse minor axis. Only the elliptical cross-sections were simulated, as comparably sized airfoils were expected to have similar electrical performance. The main purpose of this parametric analysis was to determine the general preferred major and minor axis dimensions of the antenna. The HFSS model can be seen in Figure 5.

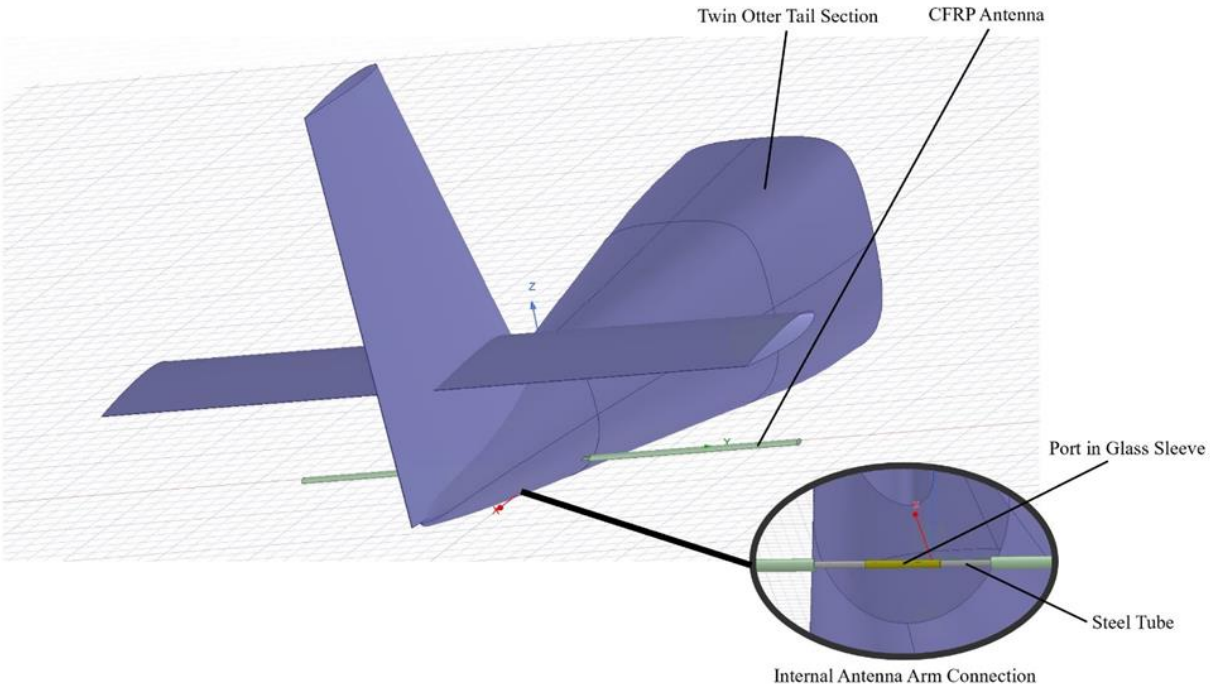

Figure 5: Antenna Internal Connection Port in Glass Sleeve

The setup included the metallic tail section of the aircraft in an attempt to capture some of the coupling effects of the aircraft. Perfect electric conductor (PEC) properties were given to the steel tube section of the antenna. The antenna included a glass sleeve over the port which was given G10 FR-4 fiberglass dielectric properties (relative dielectric loss tangent of 0.02). The glass sleeve over the dipole tube is required to isolate the antenna from the conductive airframe. The CFRP section of the antenna was given a bulk conductivity value of 8000 S/m [2]. The solution volume was modeled as a vacuum with radiation boundary conditions which maintained at least a quarter wavelength separation from any radiating surfaces. The frequency range (sweep) of the simulations was set between 10 to 40 MHz with a step size of 0.2 MHz and the antenna was excited by a 50-ohm impedance lumped port. The dimensional combinations and bandwidth of each antenna cross-section are summarized in Figure 6. The dimensions of the elliptical cross-sections

are the major and minor axes. The dimensions of the airfoil cross-sections are the thickness and chord. The length shown is for one antenna arm of the CFRP cross sections external to the aircraft.

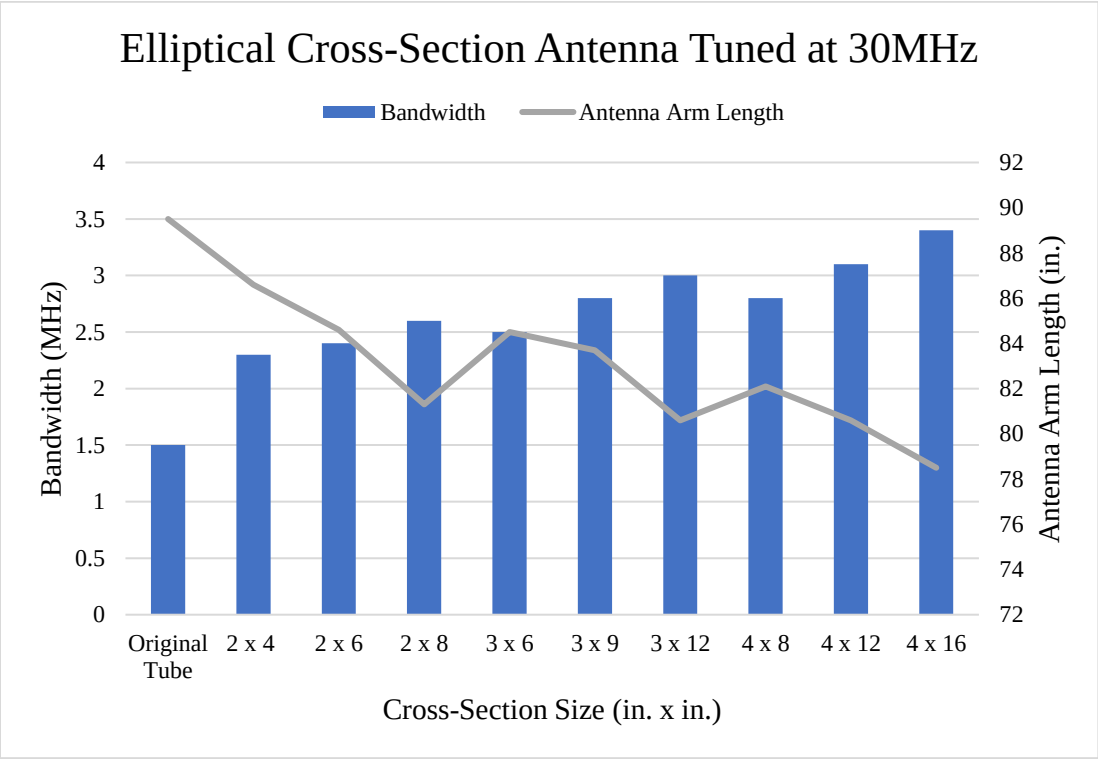

Figure 6: Elliptical Cross-Section Antenna Comparison

Note that the as-installed dipole had a larger bandwidth than the simulated dipole as shown in Figure 3, but given the difficulty in characterizing the effects of the aircraft on the antenna, it is noted that the bandwidths in Figure 6 are compared to the simulated S_{11} of the original tube in Figure 3. This was a fairer comparison between the various designs as the effect of the aircraft would be comparable. As expected, the bandwidth increased as the size of the cross-sections increased. From these initial results, the CFRP antenna with a larger cross-section appeared to have a major improvement in bandwidth compared to the original steel tube concept, with even the smallest analyzed cross-section having 1.5 times the bandwidth of the tube. Given the results

in Figure 6, it was determined to only assess the impact on vehicle performance for the 2x4, 2x6, 2x8, 3x9, and 3x12 sections as these appear to have good electrical performance and these sections would have lower drag and lift loads than the larger planform sizes.

3.2 Impact on Vehicle Range

Based on the electrical performance trade study, several of the designs were mapped to real airfoil dimensions that would closely resemble the examined elliptical shapes. This led to identifying the NACA 0024 and the Eppler 863 as potential candidates. The 3x12 and 2x8 ellipses were mapped to the NACA 0024 and the 2x6 and 3x9 section was mapped to the Eppler 863. Next, the range of the Twin Otter with and without the different antenna designs was calculated. The drag of the tube antenna used the drag coefficient (c_d) for a circular 2D cross-section from Ref. [3]. The drag of the elliptical 2x4 antenna and elliptical 3x9 antenna were determined by using the 2D drag coefficients of an elliptical rod from Ref. [8], while the 2D drag coefficients of a NACA 0024 airfoil and an Eppler 863 airfoil were taken from Ref. [9]. The drag coefficients and antenna geometries were added to a range calculator for the Twin Otter that had been used for previous missions. These range calculations took into account the total drag, including parasite drag and induced drag. The drag coefficient used in these calculations was calculated using Eqs. (1-2), where c_d is the total 2D drag coefficient, c_{d_o} is the 2D drag coefficient at zero lift, c_l is the 2D lift coefficient (at a 3^o angle of attack), AR is the aspect ratio, e is the Oswald efficiency factor (0.7 for rectangular wings), and l is the antenna arm length. The values for these variables can be seen in Table 3.

$$c_d = c_{d_o} + \frac{{c_l}^2}{\pi(AR)e} \quad \text{(Eq. 1)}$$

$$AR = \frac{l^2}{S} \quad \text{(Eq. 2)}$$

Speeds of 110 knots, 120 knots, and 140 knots were analyzed, along with altitudes of 0 ft, 5000 ft, 10000 ft, and 15000 ft. Figure 7 presents the aircraft range (in nautical miles) at sea level and 10,000 ft for a speed of 110 knots.

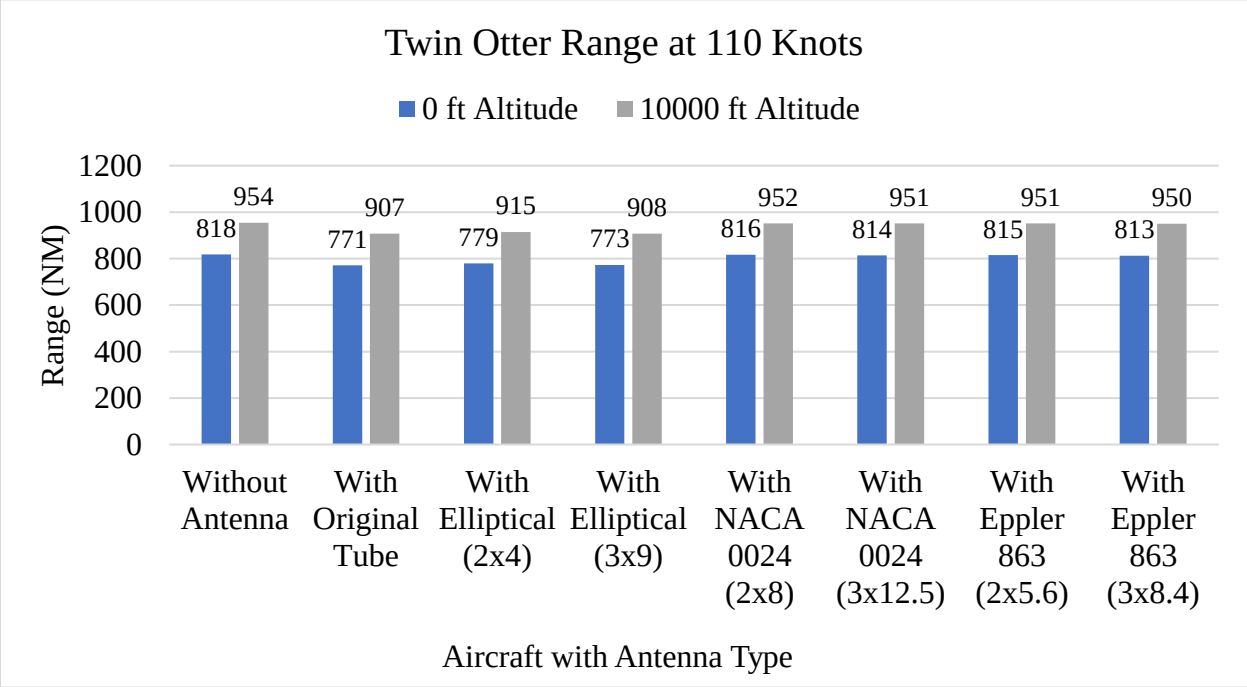

Figure 7: Twin Otter Range Comparison

On average, the range of the aircraft decreased by less than 0.6% when the NACA 0024 airfoil antenna or Eppler 863 airfoil antenna were considered. On the other hand, the range decreased by an average of 5% when the original tube antenna or elliptical antennas were added onto the aircraft. Similar relative trends across the designs were also found for the other analyzed flight conditions. Note that at lower altitudes and higher speeds, the total range for each configuration is further reduced, but the percent change in range reduction remains similar. The airfoil antennas have better range compared to the original tube antenna which would mean that using one of the airfoil antennas would improve the vehicle range during missions. After analyzing

the electrical performance and range, it was necessary to determine the structural feasibility of the designs before a candidate design could be identified, especially given the larger planform areas and improved aerodynamic characteristics.

3.3 Initial Structural Sizing

For the initial structural sizing, the flexural stress due to the aerodynamic forces was calculated, and the entire moment was assumed to be reacted by the tube inserted into the tail tie-down. The original tube was made from 4130-steel and only the drag load was considered for its stress analysis. For the aerodynamic antennas, only the lift load was considered for the flexural moment calculation. However, given that the ellipse and airfoil sections are symmetric, they theoretically will generate no lift at zero angle of attack. This was deemed unconservative, so these designs were assessed assuming an angle of attack of 5^{o}. Due to the larger planform size of the aerodynamic antennas, the resultant flexural stress exceeded the ultimate stress of the 4130-steel tube. Thus the 4130-steel tube was swapped for a stronger 52100-steel tube. However, the only commercially available 52100-steel tube that could be found has a diameter of 1.207 in. and has a thickness of 0.245 in. Thus, this size tube was used in the analysis. The properties used in this first-order analysis for both steel alloys and wet-layup AS4/epoxy plain weave carbon composite material are listed in Table 1 (4130 steel from Ref. [6] and 52100 steel from McMaster-Carr/manufacturer) and Table 2 (from Ref. [7] using the more conservative open hole allowables).

Table 1: Steel Properties

Property	4130 Steel	52100 Steel	Units
E	29×10^3	30.5×10^3	ksi
G	11×10^3	11.6×10^3	ksi
ρ	0.283	0.282	lb_f/in^3
ν	0.32	0.3	~
σ_{tu}	95	147	ksi
σ_{ty}	75	140	ksi
σ_{cy}	75	140	ksi
τ_{su}	57	~	ksi

Table 2: Biaxial Carbon Fiber Properties

Property	Value	Units
E_1	9×10^3	ksi
E_2	8.4×10^3	ksi
G_{12}	0.54×10^3	ksi
ρ	0.059	lb_f/in^3
ν_{12}	0.032	~
σ_{1t}	45	ksi
σ_{1c}	38	ksi
σ_{2t}	45	ksi
σ_{2c}	38	ksi
τ_{12}	26.5	ksi

Initially, the antennas were assumed to have a 0^o incidence angle and the stress calculations used a conservative angle of attack of 5^o. However, the resultant flexural stress was still larger than the allowable stress of the 52100-steel, so the designs were then assumed to have a -2^o incidence angle, resulting in a 3^o angle of attack used for the stress analysis. The lift load (L), stress (σ), and margin of safety (MS) calculations in Eqs. (3-5) were conducted using equations from Ref. [8] and Ref. [10] shown below.

$$L = \frac{1}{2}\rho V^2 c_l S \quad \text{(Eq. 3)}$$

$$\sigma = \frac{Mr}{I} \quad \text{(Eq. 4)}$$

$$MS = \frac{\sigma_{allowable}}{1.5*\sigma_{actual}} - 1 \quad \text{(Eq. 5)}$$

The density (ρ) used in Eq. 3 was conservatively assumed to be standard atmospheric density at sea level, 0.07654 lb_m/ft^3. The velocity (V) was assumed to be 287 ft/s, which is the never exceed velocity of the Twin Otter. The 2D coefficient of lift (c_l) for each cross section (from Ref. [8] and Ref. [9]) was used in the calculations. The lift calculation used the planform area (S) of each respective antenna design. The calculations were performed for one arm of the CFRP antenna external to the aircraft and steel tube portion. The CFRP antenna arm was assumed to be a cantilever beam. The flexural stress of each antenna design was calculated using Eq. 4. The moment (M) was calculated using the antenna arm length multiplied by the applied lift load, so it was applied as a point load at the outboard end of the antenna. The radius (r) of the tube was used

when calculating the flexural stress of the steel tube portion. The radius (r) used when calculating the flexural stress at the root of CFRP skins was half of the thickness for the airfoils and half of the minor axis for the ellipses. The second moment of area (I) of a hollow circular cross-section was used when calculating the flexural stress of the tube and a hollow elliptical cross-section was used when calculating the flexural stress at the root of the CFRP skins. The CFRP antenna was assumed to be composed of ten layers of AS4/epoxy biaxial CFRP material with a cured ply thickness of 0.0078 in. The MS of the original tube antenna came from a previously performed analysis when it was first developed. The MS calculation (Eq. 5) for the steel tube connector of the new antenna designs used the ultimate tensile strength of 52100-steel (147 ksi). The margin of safety of the CFRP antenna used the allowable compressive stress of biaxial CFRP (38 ksi). All margin of safety calculations used a 1.5 factor of safety for no fracture at the ultimate load case. Table 3 summarizes the drag coefficient, lift coefficient, and planform area used for each antenna design, along with the calculated critical margins of safety. The explicit stress and MS calculations for this initial trade study are shown in the Appendix. On average, the smaller cross-sections have lower margins of safety for the CFRP skins and the greater lifting antennas have lower margins of safety for the steel tube connector. This is due to the lift load increasing as the antenna chord is increased. A larger lift load creates a larger moment on the connection point between the CFRP and steel tube.

Table 3: Antenna Structural Sizing Comparison

Antenna Type	2D Drag Coefficient at Zero Lift (c_{d_o})	2D Lift Coefficient (c_l)	Single Antenna Arm Length (in.)	Planform Area (in.^{2})	Critical MS of CFRP Antenna Skin	Critical MS of Steel Tube
Original Tube (Diameter = 1.25 in.)	1.13	~	89.5	111.9	~	0.44
Elliptical (2 in. x 4 in.)	0.6	0.3	86.6	346.4	0.60	1.41
Elliptical (3 in. x 9 in.)	0.45	0.26	83.7	753.3	1.96	0.28
NACA 0024 (2 in. x 8 in.)	0.02	0.31	81.3	654.5	0.65	0.32
NACA 0024 (3 in. x 12.5 in.)	0.02	0.31	80.6	1007.5	1.6	-0.13
Eppler 863 (2 in. x 5.6 in.)	0.03	0.45	84.6	473.8	0.08	0.21
Eppler 863 (3 in. x 8.4 in.)	0.03	0.45	83.7	703.1	0.71	-0.18

Based on the first-order stress analysis, the two best feasible designs were the elliptical 3x9 and NACA 0024 2x8 antennas as they showed good overall performance and were the largest designs that could withstand the lift load. These two designs were carried forward into a final assessment. The final stress and natural frequencies were analyzed using a finite element analysis (FEA), the electrical performance was directly compared, and matching networks were developed for these designs to compare with the as-flown design.

4. Performance Comparison of Final Candidate Designs

4.1 Detailed Structural Design of Final Candidate Antenna Designs

The 2x8 NACA 0024 and 3x9 elliptical antenna were analyzed in MSC Patran [11] and Nastran [12] software to verify the initial stress calculations and determine that there is a feasible structural solution given the larger planform and thus larger loads. The design would be refined after a final candidate design was determined. Static, buckling, and modal finite element analyses were performed on the candidate designs. The bi-axial plain weave AS4/DPL 40 carbon fiber reinforced plastic skin was given a stacking sequence of $[0,0,0,45,0]_s$. The ribs were given a thickness of 0.2 in. for both designs, used 4130-steel properties, and were spaced 9.5 in. apart. Rib caps of 0.125 in. that used the same material as the ribs were also included in the layered composite of the model and were located against the ribs. This gave the ribs a "C-shape" with the rib caps extending towards the outboard direction. The connection tube had a diameter of 1.207 in., a thickness of 0.245 in., and used the 52100-steel properties. These parameters were selected because this is a commercially available tube and based on the initial hand calculations, it was assumed that 4130-steel would be required for the ribs and a higher strength 52100-steel would be necessary for the tube. The material properties for 4130-steel, 52100-steel, and CFRP are listed in Table 1 and Table 2, respectively. Tube placement through the rib was located at 20% of the chord length away from the leading edge and in the middle of the thickness for the NACA antenna. Tube placement through the rib was located directly in the middle of the minor and major axis for the elliptical antenna. The length of the elliptical antenna skin was 83.7 in. and the length of the NACA antenna skin was 81.3 in. The calculated lift load (at a 3^o angle of attack) for each design was applied as an upward total load to the bottom skin of the antenna (unlike in the initial calculations where it was applied as point load at the outboard end). The force was applied in this manner to

more accurately model the stresses than in the initial structural trade study. The total applied lift load was 132.2 lbs. for the ellipse and 138 lbs. for the NACA 0024. In all FEA models the limit load was analyzed within Patran, then a 1.5 factor of safety was applied in MS calculations for no fracture at ultimate load analysis. The top nodes of the rib and skin connection along with the inboard-most end of the tube were fixed in the x-direction to simulate the antenna bearing against the aircraft. The top half of the tube was fixed in the z-direction, and the middle nodes of the tube were fixed in the y-direction to simulate the antenna tube bearing against the tail tie-down tube. The applied boundary conditions can be seen in Figure 8, along with the model's coordinate system.

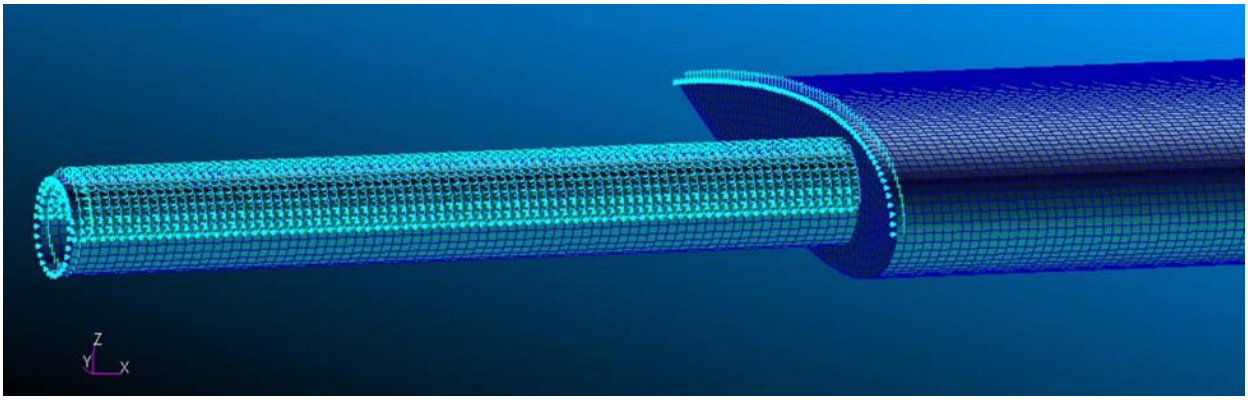

Figure 8: FEA Fixed Points

Tension, compression, and shear were examined for every static analysis performed. Only the critical stresses of each component are presented in the structural analysis and margin of safety calculations.

4.1.1 3x9 Elliptical Antenna Structural Analysis

The 3x9 elliptical airfoil model had 17104 nodes and 15567 quadrilateral elements. The element dimensions were 0.5 in. x 0.25 in. on all components except for the rib. The rib had average element dimensions of 0.25 in. x 0.25 in. The rib elements on the perimeter shared the 0.25 in. side with the skin and tube for mesh compatibility. These elements were modeled as 2D shell elements. Figure 9 and Figure 10 show that the reactionary force and moment totals balance the applied force and moment totals. Below is an estimate of the expected moment from the applied load (where M is the moment, L is the lift load, and *l* is the antenna arm length).

$$M = \frac{\left(\frac{L}{l}\right) * l^2}{2} = \frac{\left(\frac{132.2}{83.7}\right) * 83.7^2}{2} = 5532.57\ lb \cdot in.$$

The 132.2 lb. load was correctly applied, the resulting moment is at the expected value, and the applied and reactionary loads are equal and opposite, which verify the proper application of loads.

		OLOAD		RESULTANT			
SUBCASE/ DAREA ID	LOAD TYPE	T1	T2	T3	R1	R2	R3
1	FX	0.000000E+00	----	----	----	0.000000E+00	0.000000E+00
	FY	----	0.000000E+00	----	0.000000E+00	----	0.000000E+00
	FZ	----	----	1.322003E+02	-2.155798E-06	-5.532581E+03	----
	MX	----	----	----	0.000000E+00	----	----
	MY	----	----	----	----	0.000000E+00	----
	MZ	----	----	----	----	----	0.000000E+00
	TOTALS	0.000000E+00	0.000000E+00	1.322003E+02	-2.155798E-06	-5.532581E+03	0.000000E+00

Figure 9: 3x9 Ellipse Applied Loads

SPCFORCE RESULTANT

SUBCASE/ DAREA ID	LOAD TYPE	T1	T2	T3	R1	R2	R3
1	FX	1.270877E-10	----	----	----	2.757634E+03	6.581340E+00
	FY	----	4.390245E-09	----	2.356703E-02	----	-6.581339E+00
	FZ	----	----	-1.322003E+02	-2.356486E-02	2.774947E+03	----
	MX	----	----	----	0.000000E+00	----	----
	MY	----	----	----	----	0.000000E+00	----
	MZ	----	----	----	----	----	0.000000E+00
	TOTALS	1.270877E-10	4.390245E-09	-1.322003E+02	2.172810E-06	5.532581E+03	2.552773E-07

Figure 10: 3x9 Ellipse Reactionary Loads

Figure 11 shows that the epsilon value is very small, which indicates a good mesh and that the results are stable and reliable.

LOAD SEQ. NO.	EPSILON	EXTERNAL WORK	EPSILONS LARGER THAN 0.001 ARE FLAGGED WITH ASTERISKS
1	-9.4035252E-11	1.7609692E+01	

Figure 11: 3x9 Ellipse Epsilon

Figure 12 shows the thicknesses on each section of the model and verifies that the correct thicknesses were applied to each component. The blue corresponds to the layered composite, the yellow corresponds to the 4130-steel ribs, and the red corresponds to the 52100-steel tube. Table 4 summarizes the laminate layups. The composite laminate also included 4130-steel at the rib locations to model rib caps. In the table, C represents the carbon fiber biaxial cloth and St represents the 4130-steel.

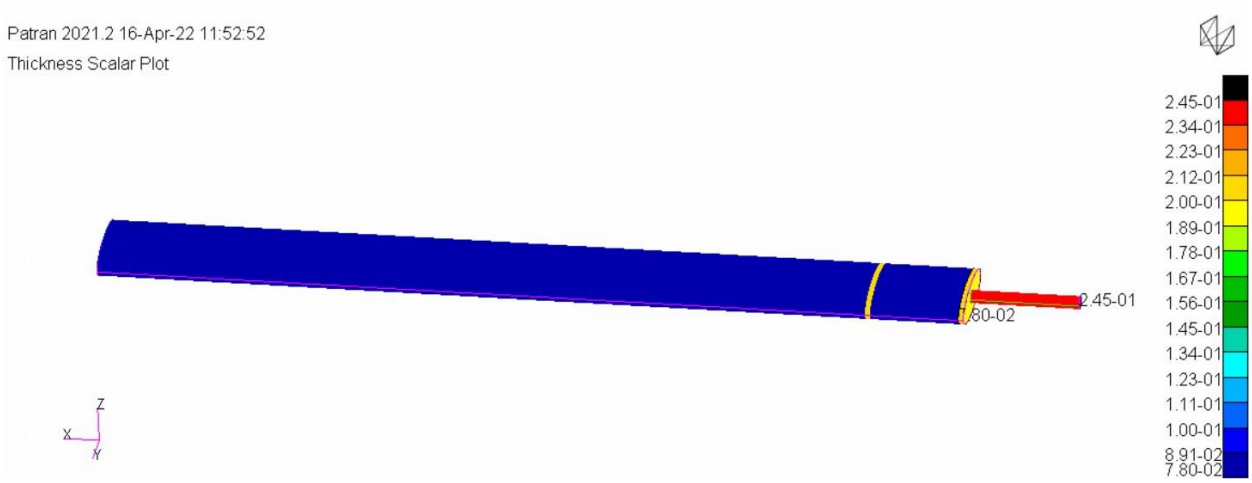

Figure 12: 3x9 Ellipse Thickness Plot

Table 4: 3x9 Ellipse Laminate Layup and Thicknesses

Laminate Color	Laminate Layup	Orientation	Laminate Thickness
Blue	[C,C,C,C,C,C,C,C,C]	$[0,0,0,45,0]_S$	0.078
Yellow (Top Skin)	[C,C,C,C,C,C,C,C,C,St]	[0,0,0,45,0,0,45,0,0,0,0]	0.203
Yellow (Bottom Skin)	[St,C,C,C,C,C,C,C,C,C]	[0,0,0,0,45,0,0,45,0,0,0]	0.203

The fringe plot in Figure 13 shows the translational displacement of the elliptical antenna. The vertical displacement verifies that the vertical lift load on the bottom half of the antenna skin was applied properly.

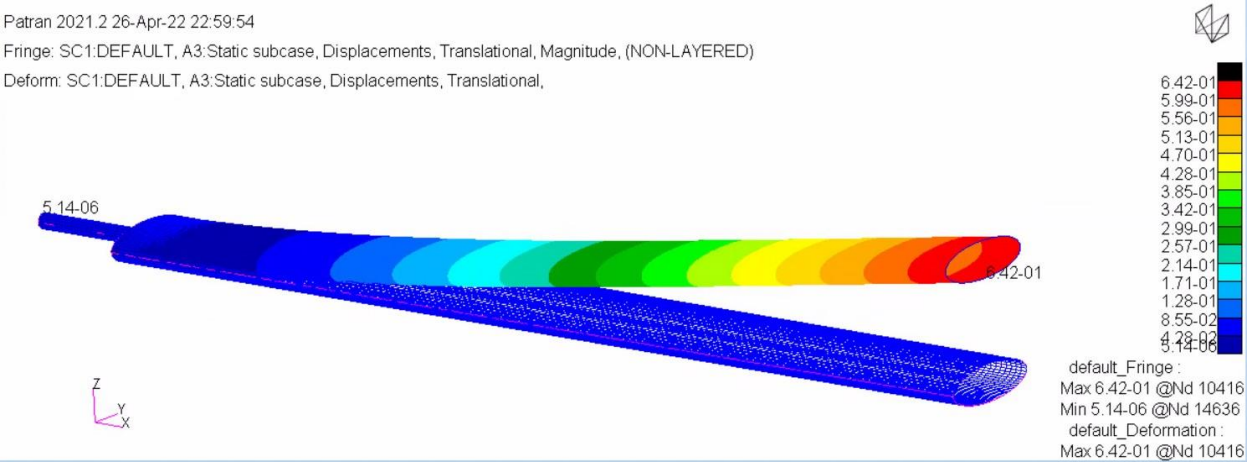

Figure 13: 3x9 Ellipse Translational Displacement

The tensor plot in Figure 14 shows the critical stress in the CFRP skin including the steel rib cap layer. The max stress was located on layer 11 which is the steel layer as seen in Figure 15. This stress is significantly lower than the stress on the steel tube and rib components and it was of more interest to know the max stress in the CFRP material, so the steel layer was omitted in the tensor plot in Figure 16. This shows the critical stress in the CFRP skin (excluding the steel layer). It is a tensile stress in the global x-direction near the inboard rib. It is located on the bottom side of the antenna skin, just under the leading edge right after the boundary conditions end (similar location as the plot with the steel layer included). The stress has a magnitude of 5.43 ksi and occurs in element 6759 on the 45^{o} ply 7 as seen in the f06 file Figure 17. The corresponding MS is calculated below. It was expected that the maximum stress would have occurred at the very top of the cross-section near the ribs. The location of the maximum stress near the leading edge is likely due to the fact that the translational constraint around the perimeter of the section ends at the leading edge resulting in a stress concentration. For this initial analysis of the structural design, this likely elevated stress was used as a conservative approach.

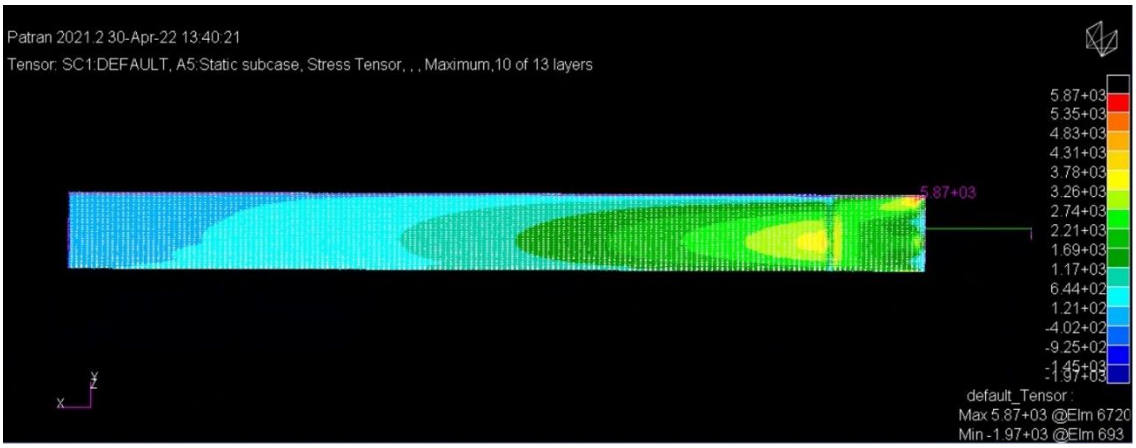

Figure 14: 3x9 Ellipse Skin Critical Stress Tensor Plot (including steel layer)

STRESSES IN LAYERED COMPOSITE ELEMENTS (QUAD4)

ELEMENT ID	PLY ID	STRESSES IN FIBER AND MATRIX DIRECTIONS NORMAL-1	NORMAL-2	SHEAR-12	INTER-LAMINAR STRESSES SHEAR XZ-MAT	SHEAR YZ-MAT	PRINCIPAL STRESSES (ZERO SHEAR) ANGLE	MAJOR	MINOR	MAX SHEAR
6720	1	5.87484E+03	-1.04775E+03	2.55032E+03	8.43293E+01	-2.65876E+02	18.19	6.71293E+03	-1.88584E+03	4.29939E+03
6720	2	2.21584E+03	6.37903E+01	1.99725E+02	7.87853E+01	-2.48456E+02	5.26	2.23422E+03	4.54115E+01	1.09441E+03
6720	3	2.25272E+03	1.64228E+02	2.08459E+02	7.24176E+01	-2.28482E+02	5.64	2.27332E+03	1.43624E+02	1.06485E+03
6720	4	2.28959E+03	2.64666E+02	2.17193E+02	6.52264E+01	-2.05954E+02	6.05	2.31262E+03	2.41632E+02	1.03550E+03
6720	5	3.18460E+03	-4.34065E+02	-1.19882E+02	6.07524E+01	-1.90953E+02	-1.90	3.18857E+03	-4.38032E+02	1.81330E+03
6720	6	2.36333E+03	4.65541E+02	2.34662E+02	5.19140E+01	-1.63318E+02	6.95	2.39192E+03	4.36956E+02	9.77480E+02
6720	7	2.40020E+03	5.65979E+02	2.43397E+02	4.22519E+01	-1.33130E+02	7.43	2.43195E+03	5.34231E+02	9.48861E+02
6720	8	3.61326E+03	-4.28939E+02	-1.06783E+02	3.63987E+01	-1.13548E+02	-1.51	3.61608E+03	-4.31758E+02	2.02392E+03
6720	9	2.47395E+03	7.66855E+02	2.60865E+02	2.50894E+01	-7.82520E+01	8.50	2.51292E+03	7.27881E+02	8.92520E+02
6720	10	2.51082E+03	8.67293E+02	2.69600E+02	1.29565E+01	-4.04028E+01	9.08	2.55391E+03	8.24198E+02	8.64858E+02
6720	11	2.54769E+03	9.67730E+02	2.78334E+02	3.55344E-14	3.17807E-14	9.70	2.59529E+03	9.20132E+02	8.37579E+02

Figure 15: 3x9 Ellipse Skin Critical Stress (including steel layer) f06

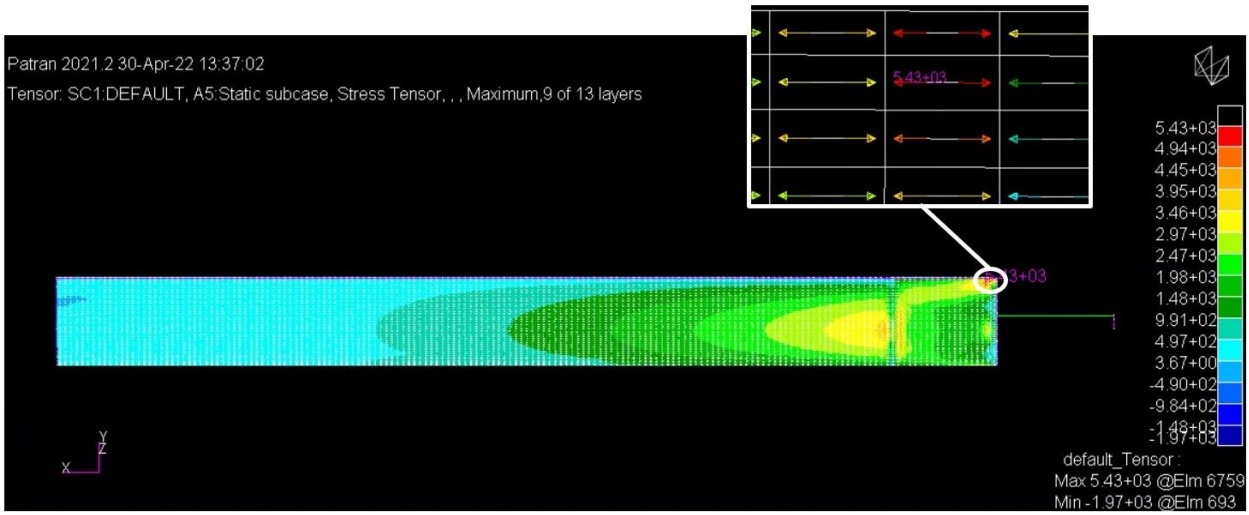

Figure 16: Ellipse Skin Critical Stress Tensor Plot (excluding steel layer)

S T R E S S E S I N L A Y E R E D C O M P O S I T E E L E M E N T S (Q U A D 4)

ELEMENT ID	PLY ID	STRESSES IN FIBER AND MATRIX DIRECTIONS NORMAL-1	NORMAL-2	SHEAR-12	INTER-LAMINAR STRESSES SHEAR XZ-MAT	SHEAR YZ-MAT	PRINCIPAL STRESSES (ZERO SHEAR) ANGLE	MAJOR	MINOR	MAX SHEAR
6759	1	4.01032E+03	-7.68695E+02	3.65244E+02	-1.55989E+01	-3.14897E+01	4.35	4.03807E+03	-7.96448E+02	2.41726E+03
6759	2	4.05830E+03	-6.61183E+02	3.73498E+02	-2.77313E+01	-5.59817E+01	4.50	4.08768E+03	-6.90558E+02	2.38912E+03
6759	3	4.10629E+03	-5.53671E+02	3.81751E+02	-3.63974E+01	-7.34759E+01	4.65	4.13735E+03	-5.84737E+02	2.36105E+03
6759	4	4.98966E+03	-1.22414E+03	-2.86771E+02	-3.92998E+01	-7.97537E+01	-2.64	5.00287E+03	-1.23735E+03	3.12011E+03
6759	5	4.20226E+03	-3.38647E+02	3.98258E+02	-4.10331E+01	-8.32526E+01	4.97	4.23692E+03	-3.73312E+02	2.30512E+03
6759	6	4.25024E+03	-2.31135E+02	4.06512E+02	-3.92998E+01	-7.97537E+01	5.14	4.28682E+03	-2.67712E+02	2.27726E+03
6759	7	5.43465E+03	-1.18195E+03	-2.74331E+02	-3.63974E+01	-7.34759E+01	-2.37	5.44600E+03	-1.19331E+03	3.31965E+03
6759	8	4.34621E+03	-1.61115E+01	4.23019E+02	-2.77313E+01	-5.59817E+01	5.49	4.38685E+03	-5.67534E+01	2.22180E+03
6759	9	4.39420E+03	9.14004E+01	4.31272E+02	-1.55989E+01	-3.14897E+01	5.67	4.43700E+03	4.85994E+01	2.19420E+03
6759	10	4.44218E+03	1.98912E+02	4.39526E+02	0.0	1.24415E-14	5.85	4.48723E+03	1.53864E+02	2.16668E+03

Figure 17: 3x9 Ellipse Skin Critical Stress (excluding steel layer) f06

$$MS_{skin} = \frac{\sigma_{allowable}}{1.5 * \sigma_{actual}} - 1 = \frac{45\ ksi}{1.5 * 5.43\ ksi} - 1 = 4.52$$

The fringe plot in Figure 18 shows the critical stress in the 52100-steel tube. It is a tensile stress on the bottom of the tube at the connecting section with the inboard rib. The stress has a magnitude of 31.6 ksi and occurs on node 16479 in element 15180 as seen in the f06 file in Figure 19. The corresponding MS is calculated below.

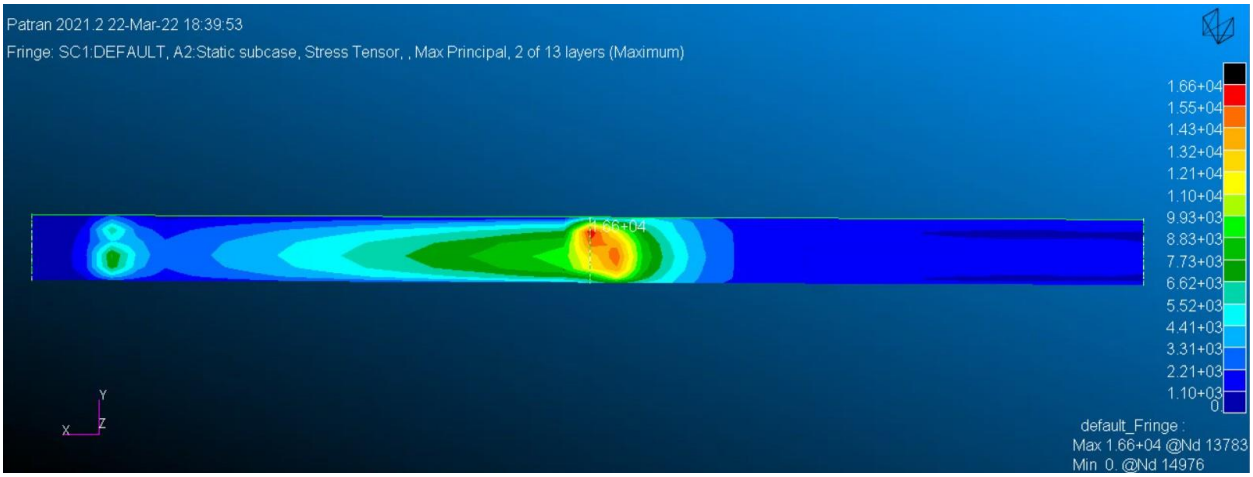

Figure 18: 3x9 Ellipse Tube Critical Stress Fringe Plot

STRESSES IN QUADRILATERAL ELEMENTS (QUAD4) OPTION = BILIN

ELEMENT ID	GRID-ID	FIBER DISTANCE	STRESSES IN ELEMENT COORD SYSTEM NORMAL-X	NORMAL-Y	SHEAR-XY	PRINCIPAL STRESSES (ZERO SHEAR) ANGLE	MAJOR	MINOR	VON MISES
15180	CEN/4	-1.000000E-01	1.297019E+04	2.549449E+04	-5.098223E+03	-70.4249	2.730739E+04	1.115729E+04	2.378029E+04
		1.000000E-01	-1.308894E+04	-2.443790E+04	3.520482E+03	15.9079	-1.208559E+04	-2.544126E+04	2.204193E+04
	13783	-1.000000E-01	1.131047E+04	2.241196E+04	-6.337851E+03	-65.6061	2.528613E+04	8.436307E+03	2.229883E+04
		1.000000E-01	-1.160084E+04	-2.197511E+04	4.586988E+03	20.7432	-9.863607E+03	-2.371234E+04	2.063193E+04
	13782	-1.000000E-01	1.102126E+04	2.792026E+04	-5.651120E+03	-73.1125	2.963586E+04	9.305667E+03	2.625068E+04
		1.000000E-01	-1.132272E+04	-2.627581E+04	4.075376E+03	14.2971	-1.028413E+04	-2.731439E+04	2.389424E+04
	16479	-1.000000E-01	1.545489E+04	3.095030E+04	-3.116824E+03	-79.0428	3.155373E+04	1.485146E+04	2.734200E+04
		1.000000E-01	-1.531412E+04	-2.878290E+04	1.826817E+03	7.5886	-1.507074E+04	-2.902628E+04	2.514368E+04
	16478	-1.000000E-01	1.477304E+04	2.142050E+04	-4.860034E+03	-62.1839	2.398465E+04	1.220889E+04	2.077244E+04
		1.000000E-01	-1.472849E+04	-2.130596E+04	3.218303E+03	22.1899	-1.341579E+04	-2.261867E+04	1.970127E+04

Figure 19: 3x9 Ellipse Tube Critical Stress f06

$$MS_{tube} = \frac{\sigma_{allowable}}{1.5 * \sigma_{actual}} - 1 = \frac{147\ ksi}{1.5 * 31.6\ ksi} - 1 = 2.10$$

The fringe plot in Figure 20 shows that the maximum critical stress was on the inboard rib which has the lowest margin of safety of all the ellipse antenna components. It is a tensile stress on the lower half of the rib near the connecting section with the tube. The stress has a magnitude of 33.5 ksi and occurs on node 13781 in element 15044 as seen in the f06 file in Figure 21. The corresponding MS is calculated below.

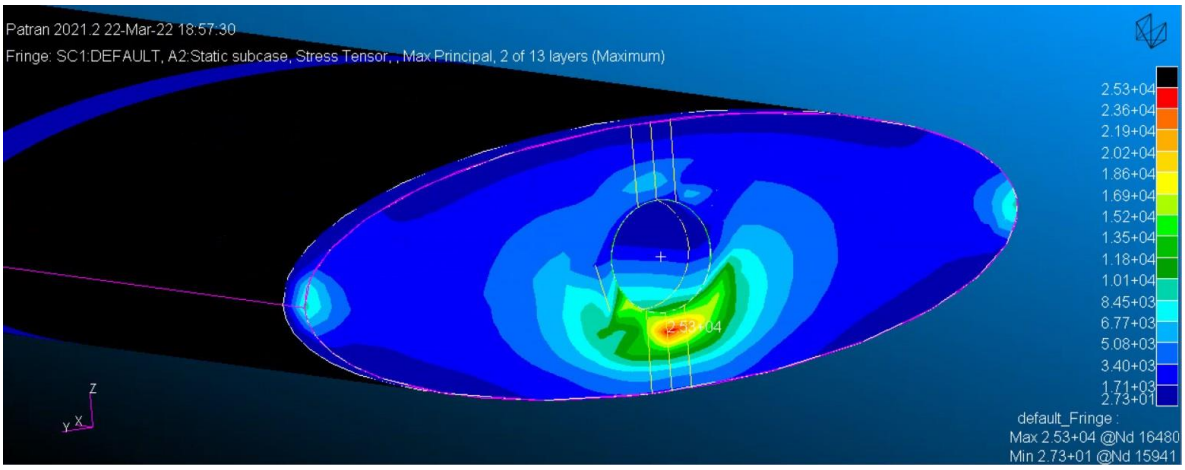

Figure 20: 3x9 Ellipse Rib Critical Stress Fringe Plot

STRESSES IN QUADRILATERAL ELEMENTS (QUAD4) OPTION = BILIN

ELEMENT ID	GRID-ID	FIBER DISTANCE	STRESSES IN ELEMENT COORD SYSTEM NORMAL-X	NORMAL-Y	SHEAR-XY	PRINCIPAL STRESSES (ZERO SHEAR) ANGLE	MAJOR	MINOR	VON MISES
15044	CEN/4	-1.000000E-01	-2.956716E+04	-1.386321E+04	4.294572E+02	88.4347	-1.385147E+04	-2.957889E+04	2.563324E+04
		1.000000E-01	3.203288E+04	1.301074E+04	-8.692342E+02	-2.6109	3.207252E+04	1.297110E+04	2.794423E+04
	16480	-1.000000E-01	-3.058454E+04	-1.652171E+04	1.370122E+02	89.4418	-1.652038E+04	-3.058587E+04	2.651656E+04
		1.000000E-01	3.350858E+04	1.609550E+04	-5.033245E+02	-1.6543	3.352311E+04	1.608097E+04	2.903984E+04
	13781	-1.000000E-01	-3.056504E+04	-1.121156E+04	5.399621E+02	88.4031	-1.119651E+04	-3.058010E+04	2.679764E+04
		1.000000E-01	3.348930E+04	9.938813E+03	-9.702135E+02	-2.3551	3.352920E+04	9.898911E+03	2.983778E+04
	13782	-1.000000E-01	-2.855684E+04	-1.133149E+04	7.116879E+02	87.6381	-1.130214E+04	-2.858619E+04	2.493639E+04
		1.000000E-01	3.056724E+04	1.007298E+04	-1.223132E+03	-3.4034	3.063998E+04	1.000024E+04	2.706300E+04
	16479	-1.000000E-01	-2.859723E+04	-1.636896E+04	3.274589E+02	88.4672	-1.636019E+04	-2.860599E+04	2.485878E+04
		1.000000E-01	3.061739E+04	1.591357E+04	-7.773463E+02	-3.0178	3.065837E+04	1.587259E+04	2.655649E+04

Figure 21: 3x9 Ellipse Rib Critical Stress f06

$$MS_{rib} = \frac{\sigma_{allowable}}{1.5 * \sigma_{actual}} - 1 = \frac{95\ ksi}{1.5 * 33.5\ ksi} - 1 = 0.89$$

A buckling analysis was performed on the elliptical antenna and it was found that the first buckling mode occurs at a load factor of 7.14 near the root of the antenna where the ribs are present as shown in Figure 22. After applying a 1.5 factor of safety, it has a margin of safety of 3.76. The corresponding MS is calculated below.

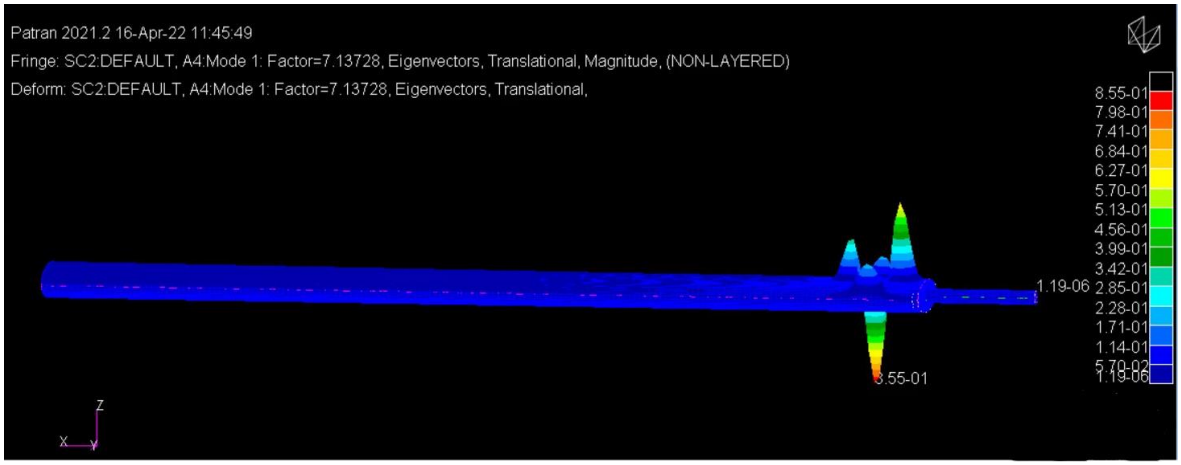

Figure 22: 3x9 Ellipse Buckling Analysis (First Mode)

$$MS_{buckling} = \frac{7.14}{1.5} - 1 = 3.76$$

4.1.2 2x8 NACA 0024 Antenna Structural Analysis

The 2x8 NACA 0024 airfoil model had 105927 nodes and 99924 quadrilateral elements. The element length was 0.125 in. on all components. These elements were modeled as 2D shell elements. Figure 23 and Figure 24 show that the reactionary force and moment totals balance the applied force and moment totals. Below is an estimate of the expected moment from the applied load (where M is the moment, L is the lift load, and *l* is the antenna arm length).

$$M = \frac{\left(\frac{L}{l}\right) * l^2}{2} = \frac{\left(\frac{138}{81.3}\right) * 81.3^2}{2} = 5609.7\ lb \cdot in.$$

The 138 lb. load was correctly applied, the resulting moment is at the expected value, and the applied and reactionary loads are equal and opposite, which verify the proper application of loads.

		OLOAD	RESULTANT				
SUBCASE/ DAREA	ID LOAD TYPE	T1	T2	T3	R1	R2	R3
1	FX	0.000000E+00	----	----	----	0.000000E+00	0.000000E+00
	FY	----	0.000000E+00	----	0.000000E+00	----	0.000000E+00
	FZ	----	----	1.379943E+02	2.558305E+02	-5.609525E+03	----
	MX	----	----	----	0.000000E+00	----	----
	MY	----	----	----	----	0.000000E+00	----
	MZ	----	----	----	----	----	0.000000E+00
	TOTALS	0.000000E+00	0.000000E+00	1.379943E+02	2.558305E+02	-5.609525E+03	0.000000E+00

Figure 23: 2x8 NACA 0024 Applied Loads

SPCFORCE RESULTANT

SUBCASE/ DAREA ID	LOAD TYPE	T1	T2	T3	R1	R2	R3
1	FX	-4.010772E-09	----	----	----	1.730498E+03	-1.557341E+02
	FY	----	2.837743E-09	----	-7.825029E-06	----	1.557341E+02
	FZ	----	----	-1.379943E+02	-2.558304E+02	3.879026E+03	----
	MX	----	----	----	0.000000E+00	----	----
	MY	----	----	----	----	0.000000E+00	----
	MZ	----	----	----	----	----	0.000000E+00
	TOTALS	-4.010772E-09	2.837743E-09	-1.379943E+02	-2.558304E+02	5.609524E+03	1.795706E-06

Figure 24: 2x8 NACA 0024 Reactionary Loads

Figure 25 shows that the epsilon value is very small, which indicates a good mesh and that the results are stable and reliable.

LOAD SEQ. NO.	EPSILON	EXTERNAL WORK	EPSILONS LARGER THAN 0.001 ARE FLAGGED WITH ASTERISKS
1	-1.2660196E-07	4.3529692E+01	

Figure 25: 2x8 NACA 0024 Epsilon

Figure 26 shows the thicknesses on each section of the model and verifies that the correct thicknesses were applied to each component. The blue corresponds to the layered composite, the yellow corresponds to the 4130-steel ribs, and the red corresponds to the 52100-steel tube. Table 5 summarizes the laminate layups. The composite laminate also included 4130-steel at the rib locations to model rib caps. In the table, C represents the carbon fiber biaxial cloth and St represents the 4130-steel.

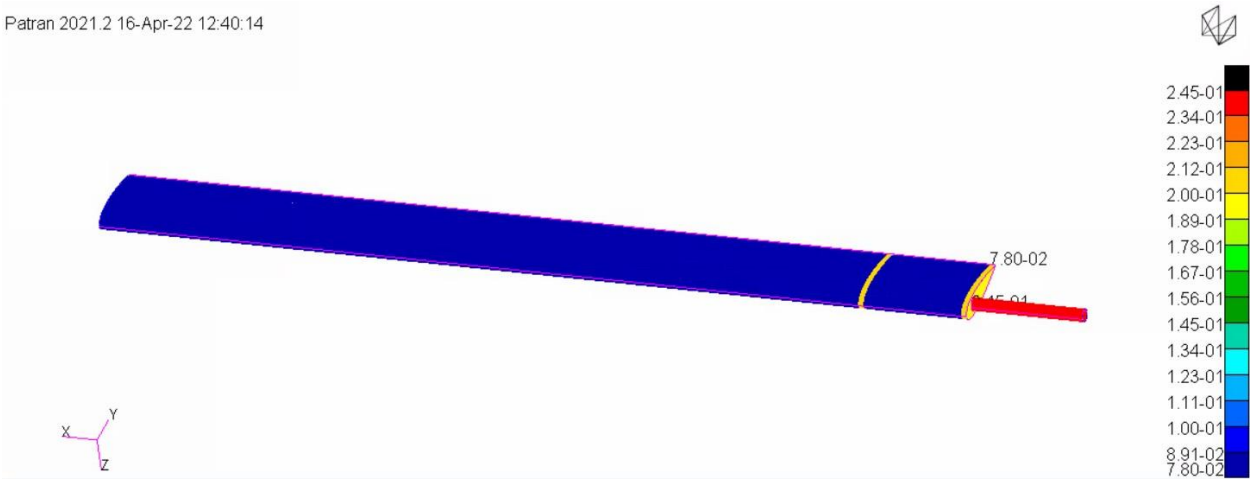

Figure 26: 2x8 NACA 0024 Thickness Plot

Table 5: 2x8 NACA 0024 Laminate Layup and Thicknesses

Laminate Color	Laminate Layup	Orientation	Laminate Thickness
Blue	[C,C,C,C,C,C,C,C,C,C]	$[0,0,0,45,0]_S$	0.078
Yellow (Top Skin)	[C,C,C,C,C,C,C,C,C,C,St]	[0,0,0,45,0,0,45,0,0,0,0]	0.203
Yellow (Bottom Skin)	[St,C,C,C,C,C,C,C,C,C,C]	[0,0,0,0,45,0,0,45,0,0,0]	0.203

The fringe plot in Figure 27 shows the translational displacement of the NACA antenna. The vertical displacement verifies that the vertical lift load on the bottom half of the antenna skin was applied properly.

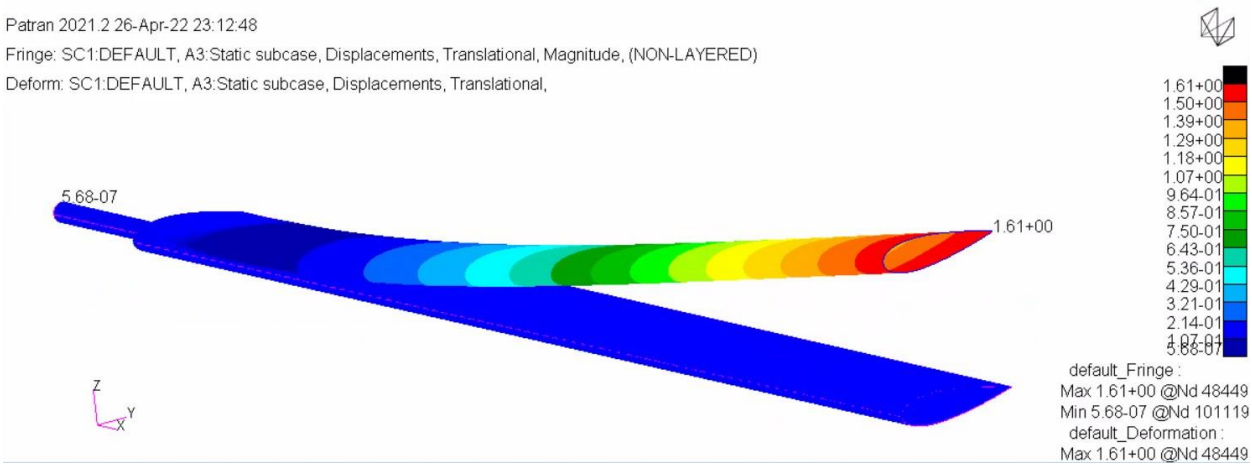

Figure 27: 2x8 NACA 0024 Translational Displacement

The tensor plot in Figure 28 shows the critical stress in the CFRP skin. It is a tensile stress in the global x-direction on the bottom where the outer rib sits. The stress has a magnitude of 9.73 ksi and occurs in element 8871 on the 0^o ply 10 as seen in the f06 file in Figure 29. Because there are only two ribs, all the stress in the skin is shearing into the rib at this location, thus causing a stress concentration that results in stress levels higher than at the root. The corresponding MS is calculated below.

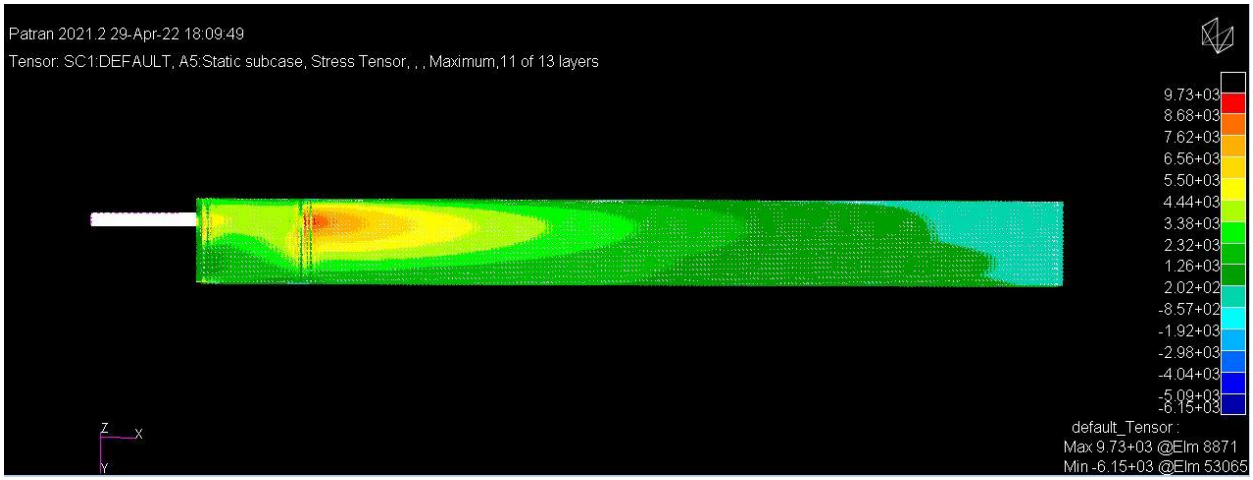

Figure 28: 2x8 NACA 0024 Skin Critical Stress Tensor Plot

S T R E S S E S I N L A Y E R E D C O M P O S I T E E L E M E N T S (Q U A D 4)

ELEMENT ID	PLY ID	STRESSES IN FIBER AND MATRIX DIRECTIONS NORMAL-1	NORMAL-2	SHEAR-12	INTER-LAMINAR STRESSES SHEAR XZ-MAT	SHEAR YZ-MAT	PRINCIPAL STRESSES (ZERO SHEAR) ANGLE	MAJOR	MINOR	MAX SHEAR
8871	1	8.79229E+03	-1.87246E+03	2.87961E+01	-1.02490E+01	2.06359E+01	0.15	8.79237E+03	-1.87254E+03	5.33245E+03
8871	2	8.89702E+03	-1.85613E+03	2.41800E+01	-1.82204E+01	3.66860E+01	0.13	8.89708E+03	-1.85619E+03	5.37663E+03
8871	3	9.00175E+03	-1.83981E+03	1.95640E+01	-2.39143E+01	4.81504E+01	0.10	9.00179E+03	-1.83984E+03	5.42082E+03
8871	4	3.68755E+03	3.22306E+03	-6.84599E+02	-2.58213E+01	5.22644E+01	-35.63	4.17823E+03	2.73239E+03	7.22919E+02
8871	5	9.21122E+03	-1.80716E+03	1.03318E+01	-2.69601E+01	5.45573E+01	0.05	9.21123E+03	-1.80717E+03	5.50920E+03
8871	6	9.31595E+03	-1.79084E+03	5.71576E+00	-2.58213E+01	5.22644E+01	0.03	9.31595E+03	-1.79084E+03	5.55340E+03
8871	7	3.75849E+03	3.49858E+03	-7.00811E+02	-2.39143E+01	4.81504E+01	-39.75	4.34129E+03	2.91577E+03	7.12759E+02
8871	8	9.52541E+03	-1.75819E+03	-3.51638E+00	-1.82204E+01	3.66860E+01	-0.02	9.52541E+03	-1.75819E+03	5.64180E+03
8871	9	9.63014E+03	-1.74187E+03	-8.13245E+00	-1.02490E+01	2.06359E+01	-0.04	9.63014E+03	-1.74187E+03	5.68601E+03
8871	10	9.73487E+03	-1.72554E+03	-1.27485E+01	0.0	-8.15319E-15	-0.06	9.73488E+03	-1.72556E+03	5.73022E+03
8872	1	8.59289E+03	-1.80966E+03	-6.57578E+01	-1.11418E+01	3.10803E+01	-0.36	8.59331E+03	-1.81007E+03	5.20169E+03

Figure 29: 2x8 NACA 0024 Skin Critical Stress f06

$$MS_{skin} = \frac{\sigma_{allowable}}{1.5 * \sigma_{actual}} - 1 = \frac{45\ ksi}{1.5 * 9.73\ ksi} - 1 = 2.08$$

The fringe plot in Figure 30 shows the critical stress in the 52100-steel tube. It is a tensile stress on the bottom of the tube at the connecting section with the inboard rib. The stress has a magnitude of 32.9 ksi and occurs on node 101151 in element 95515 as seen in the f06 file Figure 31. The corresponding MS is calculated below.

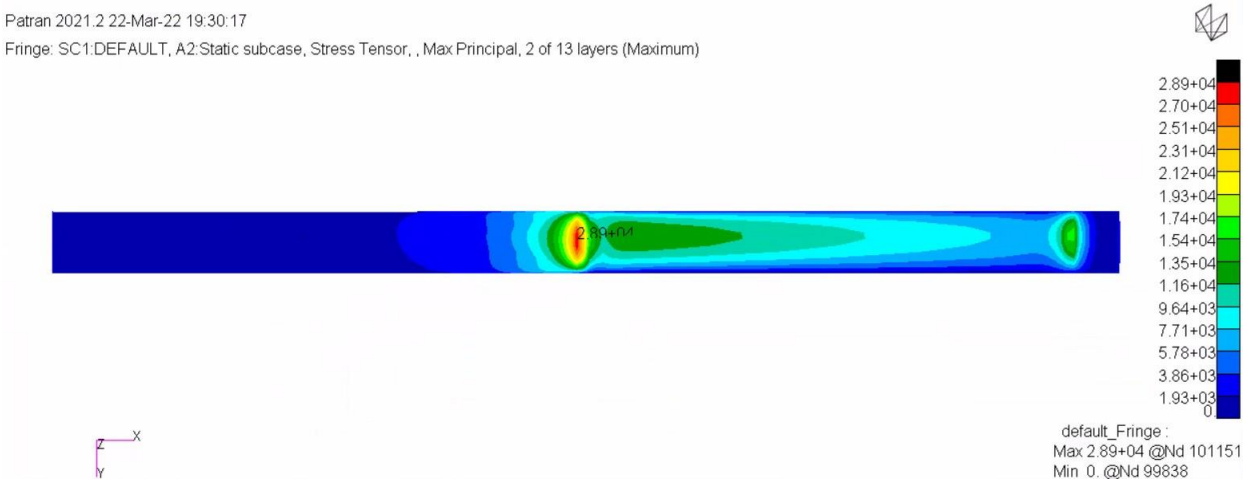

Figure 30: 2x8 NACA 0024 Tube Critical Stress Fringe Plot

STRESSES IN QUADRILATERAL ELEMENTS (QUAD4) OPTION = BILIN

ELEMENT ID	GRID-ID	FIBER DISTANCE	STRESSES IN ELEMENT COORD SYSTEM NORMAL-X	NORMAL-Y	SHEAR-XY	PRINCIPAL STRESSES (ZERO SHEAR) ANGLE	MAJOR	MINOR	VON MISES
95515	CEN/4	-1.225000E-01	7.859942E+03	3.256439E+04	-6.878592E-01	-89.9984	3.256439E+04	7.859942E+03	2.943237E+04
		1.225000E-01	-3.680492E+02	-3.417570E+03	7.791087E+01	1.4626	-3.660600E+02	-3.419559E+03	3.252018E+03
	97855	-1.225000E-01	7.646607E+03	3.285776E+04	-6.936198E-01	-89.9984	3.285776E+04	7.646607E+03	2.978007E+04
		1.225000E-01	-4.409110E+02	-3.420631E+03	7.791613E+01	1.4969	-4.388749E+02	-3.422667E+03	3.225700E+03
	97854	-1.225000E-01	7.646607E+03	3.227103E+04	-6.525772E-01	-89.9985	3.227103E+04	7.646607E+03	2.920832E+04
		1.225000E-01	-4.409108E+02	-3.414509E+03	7.791570E+01	1.4999	-4.388707E+02	-3.416549E+03	3.219626E+03
	101152	-1.225000E-01	8.073294E+03	3.227096E+04	-6.820950E-01	-89.9984	3.227096E+04	8.073294E+03	2.908711E+04
		1.225000E-01	-2.951821E+02	-3.414508E+03	7.790562E+01	1.4298	-2.932376E+02	-3.416452E+03	3.279680E+03
	101151	-1.225000E-01	8.073294E+03	3.285783E+04	-7.231469E-01	-89.9983	3.285783E+04	8.073294E+03	2.965711E+04
		1.225000E-01	-2.951820E+02	-3.420632E+03	7.790605E+01	1.4270	-2.932412E+02	-3.422573E+03	3.285781E+03

Figure 31: 2x8 NACA 0024 Tube Critical Stress f06

$$MS_{tube} = \frac{\sigma_{allowable}}{1.5 * \sigma_{actual}} - 1 = \frac{147\ ksi}{1.5 * 32.9\ ksi} - 1 = 1.98$$

The fringe plot in Figure 32 shows that the maximum critical stress was on the inboard rib which has the lowest margin of safety of all the NACA 0024 antenna components. It is a tensile stress on the lower half of the rib at the connecting section with the tube. This location is similar to where the elliptical antenna was experiencing the most stress. The stress has a magnitude of 35.3 ksi and occurs on node 97853 in element 92376 as seen in the f06 file in Figure 33. The corresponding MS is calculated below.

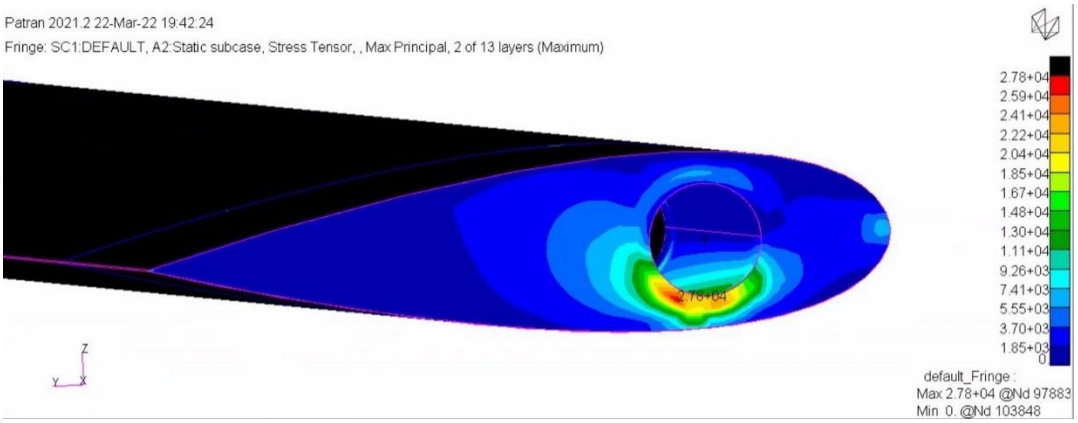

Figure 32: 2x8 NACA 0024 Rib Critical Stress Fringe Plot

STRESSES IN QUADRILATERAL ELEMENTS (QUAD4) OPTION = BILIN

ELEMENT ID	GRID-ID	FIBER DISTANCE	STRESSES IN ELEMENT COORD SYSTEM NORMAL-X	NORMAL-Y	SHEAR-XY	PRINCIPAL STRESSES (ZERO SHEAR) ANGLE	MAJOR	MINOR	VON MISES
92376	CEN/4	-1.000000E-01	3.252415E+04	1.119940E+04	1.036939E+03	2.7773	3.257445E+04	1.114910E+04	2.867440E+04
		1.000000E-01	-2.900693E+04	-1.326428E+04	1.479552E+03	84.6772	-1.312643E+04	-2.914478E+04	2.528150E+04
	97853	-1.000000E-01	3.527826E+04	8.832033E+03	9.464565E+02	2.0470	3.531209E+04	8.798204E+03	3.183817E+04
		1.000000E-01	-3.062974E+04	-1.106227E+04	1.493740E+03	85.6597	-1.094890E+04	-3.074311E+04	2.698915E+04
	97883	-1.000000E-01	3.464806E+04	1.339864E+04	7.720345E+02	2.0780	3.467608E+04	1.337063E+04	3.029130E+04
		1.000000E-01	-3.026163E+04	-1.530104E+04	1.671801E+03	83.7009	-1.511649E+04	-3.044617E+04	2.636737E+04
	97882	-1.000000E-01	3.046941E+04	1.321281E+04	1.092459E+03	3.6080	3.053830E+04	1.314392E+04	2.653219E+04
		1.000000E-01	-2.779642E+04	-1.513650E+04	1.480103E+03	83.4196	-1.496576E+04	-2.796716E+04	2.424017E+04
	97852	-1.000000E-01	2.981834E+04	8.963941E+03	1.346965E+03	3.6803	2.990498E+04	8.877302E+03	2.660148E+04
		1.000000E-01	-2.740894E+04	-1.119500E+04	1.260144E+03	85.5823	-1.109765E+04	-2.750629E+04	2.396870E+04

Figure 33: 2x8 NACA 0024 Rib Critical Stress f06

$$MS_{rib} = \frac{\sigma_{allowable}}{1.5 * \sigma_{actual}} - 1 = \frac{95\ ksi}{1.5 * 35.3\ ksi} - 1 = 0.79$$

A buckling analysis was performed on the NACA antenna and it was found that the first buckling mode occurs at a load factor of 3.25 near the root of the antenna closest to the outer rib as shown in Figure 34. After applying a 1.5 factor of safety, it has a margin of safety of 1.17. The corresponding MS is calculated below.

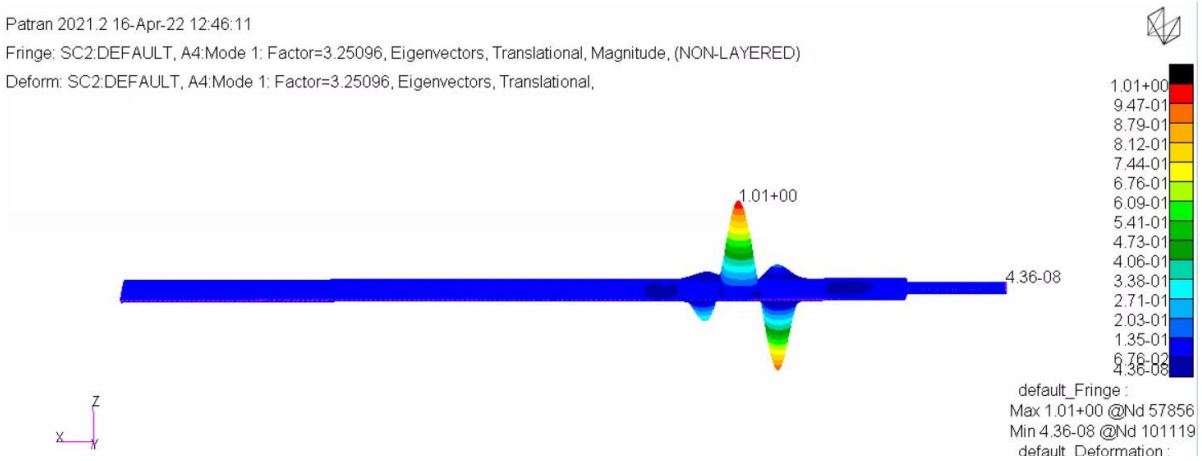

Figure 34: 2x8 NACA 0024 Buckling Analysis (First Mode)

$$MS_{buckling} = \frac{3.25}{1.5} - 1 = 1.17$$

4.1.3 Candidate Design Structural Analysis Summary and Comparison

The critical stresses for the tube, skin, and ribs were all in tension for both antennas. The critical stress in the CFRP skin was in the global x-direction for both antennas. The critical margins of safety from the static and buckling FEA can be seen in Table 6. Based on the FEA, it appears that the presented designs are feasible and would meet structural requirements.

Table 6: FEA Critical Margins of Safety

	NACA 0024 2x8in	**Elliptical 3x9in**
Tube Critical Margin of Safety	1.98	2.10
Rib Critical Margin of Safety	0.79	0.89
Skin Critical Margin of Safety	2.08	4.52
Buckling Critical Margin of Safety	1.17	3.76

In addition to meeting structural requirements, the natural frequencies of the antennas needed to be outside of the Twin Otter's blade passage frequency. Their natural frequencies were analyzed to determine this. The natural frequencies of both antennas are listed in Table 7. The natural frequencies of the original antenna were calculated using the weighted frequencies of a clamped-free cantilever beam found in Ref. [13]. The natural frequencies of the NACA 0024 and

elliptical antennas were taken from a modal FEA performed in Patran and Nastran. The 2x8 NACA 0024 antenna and the 3x9 elliptical antenna still have low first modes like the original tube antenna, but they are 2.5-3.5 times higher than the tube antenna. The higher frequency first modes are advantageous because lower frequency modes require little energy to excite. The NACA antenna has a large gap in frequencies around the 110 Hz blade passage frequency of the aircraft which is ideal for the dynamic response of the structure. The elliptical antenna has a natural frequency that is within 6 Hz of the blade passage frequency which would need to be verified experimentally given its close proximity to the blade passage frequency.

Table 7: Natural Frequency Comparison

	Original Tube	**NACA 0024 2x8in**	**Elliptical 3x9in**
Mode 1	5.6 Hz	14.3 Hz	20.1 Hz
Mode 2	35.2 Hz	47.8 Hz	49.5 Hz
Mode 3	98.4 Hz	79.7 Hz	115.7 Hz
Mode 4	177.0 Hz	142.9 Hz	153.8 Hz
Mode 5	192.8 Hz	178.3 Hz	197.8 Hz

The original antenna weight was 10.6 lbs. for one arm. The expected weight of the 3 in. x 9 in. elliptical antenna is 16.3 lbs. for one arm and the expected weight of the 2 in. x 8 in. NACA 0024 is 13.5 lbs. for one arm. The weights are comparable, though the vehicle is not weight critical.

4.2 Final Expected Electrical Performance

Given that this study was driven by the desire to increase the bandwidth of the existing antenna, here the simulated results for the three antenna designs are presented. Though the simulated tube bandwidth was smaller than the installed bandwidth (as shown in Figure 3), it was used in the comparison since the aircraft integration effects are expected to be similar between the various designs. Given that only simulated results are available for the aerodynamic antennas, it would have been unfair to compare them to the actual tube antenna performance. The simulated S_{11} of the tube, ellipse, and NACA 0024 antennas are shown in Figure 35. The 2x8 NACA 0024 and 3x9 elliptical antennas were tuned to resonate at 30 MHz. The electrical simulation in HFSS showed that the NACA 0024 antenna has a bandwidth of 2.6 MHz and the elliptical antenna has a bandwidth of 2.8 MHz. The simulated resonant frequency of the original antenna was 30.4 MHz and it had a bandwidth of 1.5 MHz, meaning that the aerodynamic antennas exhibit roughly 1.75 times the bandwidth as the original antenna.

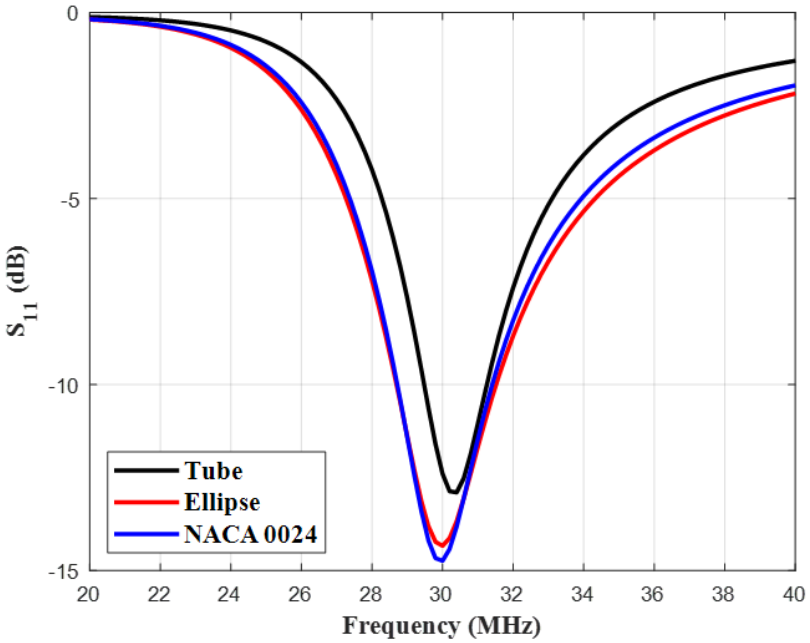

Figure 35: Simulated S_{11} Comparison of Original, 2x8 NACA, and 3x9 Elliptical Antennas

Since the final design of the antenna will include an impedance matching network, MNs were designed and simulated for each of the three designs. Fifth order LC impedance MNs were synthesized using Keysight Genesys [14]. Figure 36 shows the response of the antennas with their respective MNs. As the figure shows, the tube with MN was expected to have a 10-dB impedance bandwidth of 7.7 MHz, while the ellipse and airfoil exhibit bandwidths of 11 MHz and 10.6 MHz, respectively. Based on the simulation, the two candidate designs are expected improve the bandwidth by at least 3 MHz, or almost 40%.

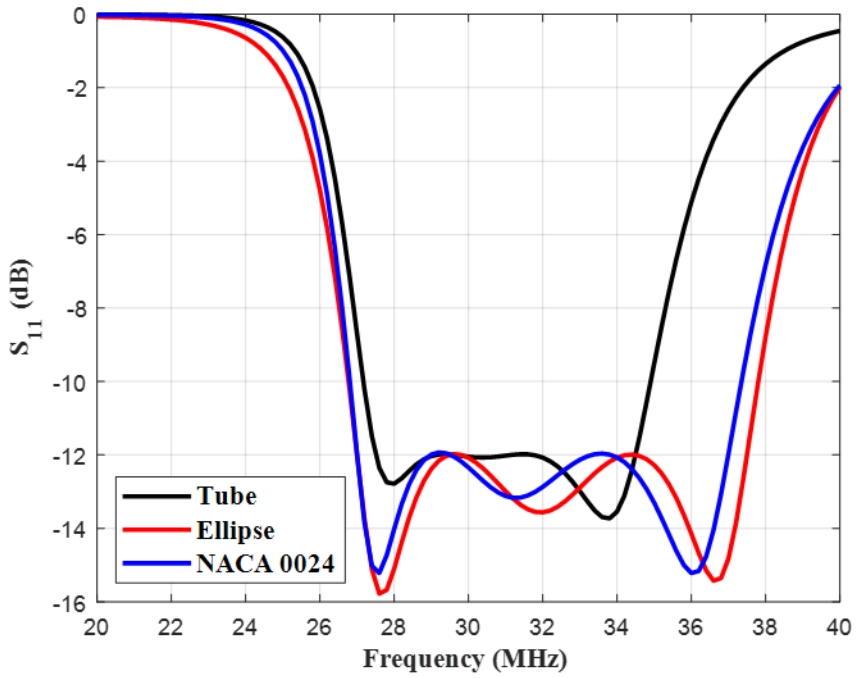

Figure 36: Comparison of Antenna Designs with MNs

4.3 Final Design and Structural Analysis

Based on all analyzed conditions, the 2 in. x 8 in. NACA 0024 antenna was selected as the final candidate design. Both candidates appeared to have feasible structural solutions, but the

NACA antenna showed better vehicle range than the elliptical antenna and the original tube antenna while also showing better electrical performance than the tube antenna and almost equivalent electrical performance to the elliptical antenna. After further assessment, a 3^o angle of attack appeared too unconservative, so for the final design of the 2x8 NACA 0024 antenna, a more rigorous sizing approach was undertaken to analyze at a 5^o angle of attack and still using the never exceed velocity (V_{ne}) of the Twin Otter. This resulted in a lift load of 221 lbs. The angle of attack may change during flight, so other potential load conditions were calculated to compare different lift loads. These potential load conditions are shown in Table 8. The calculation for each lift load is in the Appendix. Load case 1 will be analyzed within this section. Load case 2 was analyzed in Section 4.1.1 and Section 4.1.2 for the previous 2x8 NACA 0024 design and the 3x9 elliptical design. Load case 3 is essentially a stall condition for the aircraft with a high angle of attack. Load case 4 represents a potential takeoff condition. Load case 5 is 1.2 times load case 3 to represent a minimum takeoff safety condition. Each of these analyzed conditions produce a lift load that is smaller than the lift load of the 5^o never exceed velocity condition, which is a good sign that the aircraft could withstand multiple different loading conditions in flight.

Table 8: Potential Load Conditions

Load Case	Angle of Attack	Velocity (ft/s)	Lift Load (lbs.)
1	5^o	287 (V_{ne})	221
2	3^o	287 (V_{ne})	138
3	15^o	111 (minimum control velocity [V_{mc}])	83
4	10^o	190 (an average cruise velocity)	185
5	15^o	133 (1.2*V_{mc})	119

From the previous FEA, it was recognized that the stresses on the antenna, in particular the tube, were not as high as previously thought from the initial calculations, so 4130-steel was used for the tube in this analysis. The tube remained the same dimensions and thicknesses. The rib still used 4130-steel and maintained the 0.125 in. rib caps, but the overall rib thickness had to be increased to 0.25 in. due to the larger load imposed by the larger angle of attack. The number of plies and stacking sequence of the CFRP remained the same as well. Static, buckling, and modal finite element analyses were performed on this final 2x8 NACA 0024 antenna to determine the stresses on the structure and its natural frequencies. Tension, compression, and shear were examined for every static analysis performed. Only the critical stresses of each component are presented in the structural analysis and margin of safety calculations.

The FEA used the same constraints as the original 2x8 NACA 0024 model. The total upward lift load applied to the bottom skin was 221 lbs. The final 2x8 NACA 0024 antenna model had 105927 nodes and 99924 quadrilateral elements. The element length was 0.125 in. on all components. These elements were modeled as 2D shell elements. Figure 37 and Figure 38 show that the reactionary force and moment totals balance the applied force and moment totals. Below is an estimate of the expected moment from the applied load (where M is the moment, L is the lift load, and *l* is the antenna arm length).

$$M = \frac{\left(\frac{L}{l}\right) * l^2}{2} = \frac{\left(\frac{221}{81.3}\right) * 81.3^2}{2} = 8983.65\ lb \cdot in.$$

The 221 lb. load was correctly applied, the resulting moment is at the expected value, and the applied and reactionary loads are equal and opposite, which verify the proper application of loads.

OLOAD RESULTANT

SUBCASE/ DAREA ID	LOAD TYPE	T1	T2	T3	R1	R2	R3
1	FX	0.000000E+00	----	----	----	0.000000E+00	0.000000E+00
	FY	----	0.000000E+00	----	0.000000E+00	----	0.000000E+00
	FZ	----	----	2.209909E+02	4.096996E+02	-8.983371E+03	----
	MX	----	----	----	0.000000E+00	----	----
	MY	----	----	----	----	0.000000E+00	----
	MZ	----	----	----	----	----	0.000000E+00
	TOTALS	0.000000E+00	0.000000E+00	2.209909E+02	4.096996E+02	-8.983371E+03	0.000000E+00

Figure 37: Final NACA 0024 Applied Loads

SPCFORCE RESULTANT

SUBCASE/ DAREA ID	LOAD TYPE	T1	T2	T3	R1	R2	R3
1	FX	-4.917339E-09	----	----	----	2.951798E+03	-3.228003E+02
	FY	----	-5.356067E-08	----	-1.844710E-05	----	3.228003E+02
	FZ	----	----	-2.209909E+02	-4.096995E+02	6.031573E+03	----
	MX	----	----	----	0.000000E+00	----	----
	MY	----	----	----	----	0.000000E+00	----
	MZ	----	----	----	----	----	0.000000E+00
	TOTALS	-4.917339E-09	-5.356067E-08	-2.209909E+02	-4.096996E+02	8.983371E+03	-4.214332E-06

Figure 38: Final NACA 0024 Reactionary Loads

Figure 39 shows that the epsilon value is very small, which indicates a good mesh and that the results are stable and reliable.

LOAD SEQ. NO.	EPSILON	EXTERNAL WORK	EPSILONS LARGER THAN 0.001 ARE FLAGGED WITH ASTERISKS
1	-1.1629691E-07	1.1135631E+02	

Figure 39: Final NACA 0024 Epsilon

Figure 40 shows the thicknesses on each section of the model and verifies that the correct thicknesses were applied to each component. The blue corresponds to the layered composite and the red corresponds to the 4130-steel tube and ribs. The composite laminate also included 4130-steel at the rib locations to model rib caps (corresponding color in yellow). Table 9 summarizes

the laminate layups. In the table, C represents the carbon fiber biaxial cloth and St represents the 4130-steel.

Figure 40: Final NACA 0024 Thickness Plot

Table 9: Final NACA 0024 Laminate Layup and Thicknesses

Laminate Color	Laminate Layup	Orientation	Laminate Thickness
Blue	[C,C,C,C,C,C,C,C,C,C]	$[0,0,0,45,0]_S$	0.078
Yellow (Top Skin)	[C,C,C,C,C,C,C,C,C,C,St]	[0,0,0,45,0,0,45,0,0,0,0]	0.203
Yellow (Bottom Skin)	[St,C,C,C,C,C,C,C,C,C,C]	[0,0,0,0,45,0,0,45,0,0,0]	0.203

The fringe plot in Figure 41 shows the translational displacement of the final NACA antenna. The vertical displacement verifies that the vertical lift load on the bottom half of the antenna skin was applied properly.

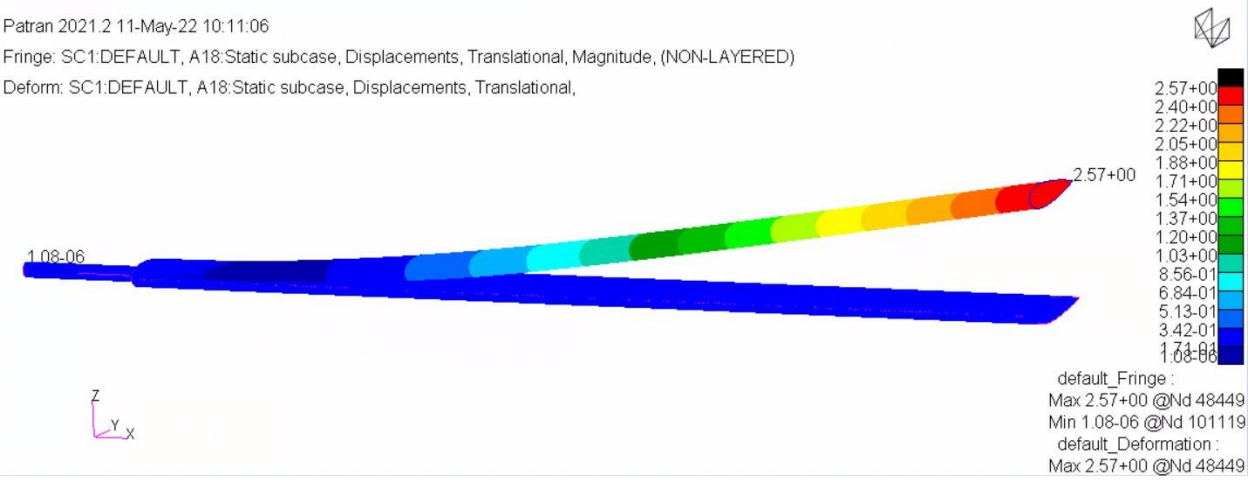

Figure 41: Final NACA 0024 Translational Displacement

The tensor plot in Figure 42 shows the critical stress in the CFRP skin. It is a compressive stress in the global x-direction on the bottom where the outer rib sits. The stress has a magnitude of 15.7 ksi and occurs in element 53070 on the 0^{o} ply 10 as seen in the f06 file in Figure 43. Because there are only two ribs, all the stress in the skin is shearing into the rib at this location, thus causing a stress concentration that results in stress levels higher than at the root. The corresponding MS is calculated below.

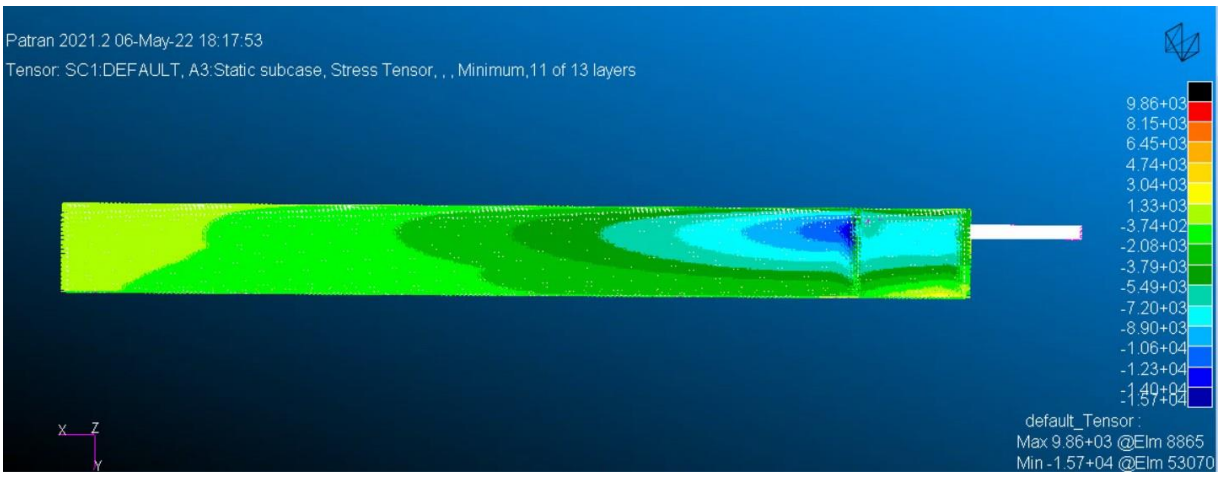

Figure 42: Final NACA 0024 Skin Critical Stress Tensor Plot

S T R E S S E S I N L A Y E R E D C O M P O S I T E E L E M E N T S (Q U A D 4)

ELEMENT ID	PLY ID	STRESSES IN FIBER AND MATRIX DIRECTIONS NORMAL-1	NORMAL-2	SHEAR-12	INTER-LAMINAR STRESSES SHEAR XZ-MAT	SHEAR YZ-MAT	PRINCIPAL STRESSES (ZERO SHEAR) ANGLE	MAJOR	MINOR	MAX SHEAR
53070	1	-1.13566E+04	1.34911E+03	-1.35031E+02	3.71463E+01	1.65781E+01	-89.39	1.35055E+03	-1.13580E+04	6.35428E+03
53070	2	-1.18422E+04	1.34635E+03	-1.37139E+02	6.60378E+01	2.94722E+01	-89.40	1.34778E+03	-1.18436E+04	6.59570E+03
53070	3	-1.23278E+04	1.34359E+03	-1.39246E+02	8.66746E+01	3.86823E+01	-89.42	1.34501E+03	-1.23293E+04	6.83713E+03
53070	4	-6.81856E+03	-4.24210E+03	8.82181E+02	9.35864E+01	4.19873E+01	72.80	-3.96899E+03	-7.09167E+03	1.56134E+03
53070	5	-1.32991E+04	1.33808E+03	-1.43462E+02	9.77138E+01	4.38294E+01	-89.44	1.33948E+03	-1.33005E+04	7.31999E+03
53070	6	-1.37847E+04	1.33532E+03	-1.45569E+02	9.35864E+01	4.19873E+01	-89.45	1.33672E+03	-1.37861E+04	7.56142E+03
53070	7	-7.60105E+03	-4.87843E+03	9.71844E+02	8.66746E+01	3.86823E+01	72.24	-4.56713E+03	-7.91236E+03	1.67262E+03
53070	8	-1.47560E+04	1.32980E+03	-1.49785E+02	6.60378E+01	2.94722E+01	-89.47	1.33120E+03	-1.47574E+04	8.04429E+03
53070	9	-1.52416E+04	1.32704E+03	-1.51892E+02	3.71463E+01	1.65781E+01	-89.47	1.32844E+03	-1.52430E+04	8.28573E+03
53070	10	-1.57273E+04	1.32429E+03	-1.54000E+02	0.0	-6.54997E-15	-89.48	1.32568E+03	-1.57286E+04	8.52716E+03

Figure 43: Final NACA 0024 Skin Critical Stress f06

$$MS_{skin} = \frac{\sigma_{allowable}}{1.5 * \sigma_{actual}} - 1 = \frac{38\ ksi}{1.5 * 15.7\ ksi} - 1 = 0.61$$

The fringe plot in Figure 44 shows the critical stress in the 4130-steel tube. It is a tensile stress on the bottom of the tube at the connecting section with the inboard rib. The stress has a magnitude of 53.6 ksi and occurs on node 101151 in element 95515 as seen in the f06 file in Figure 45. The corresponding MS is calculated below.

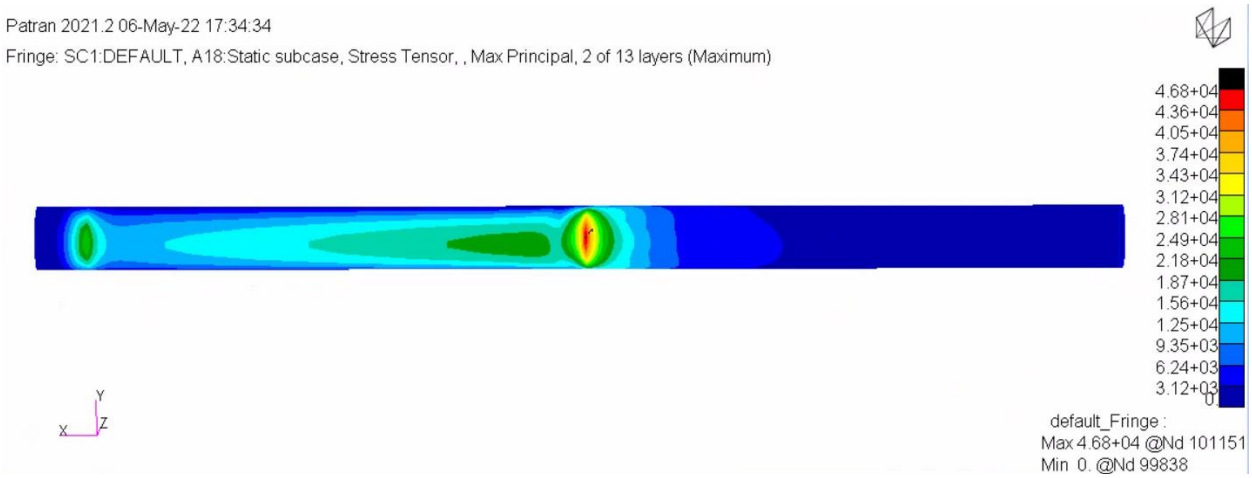

Figure 44: Final NACA 0024 Tube Critical Stress Fringe Plot

STRESSES IN QUADRILATERAL ELEMENTS (QUAD4) OPTION = BILIN

ELEMENT ID	GRID-ID	FIBER DISTANCE	STRESSES IN ELEMENT COORD SYSTEM NORMAL-X	NORMAL-Y	SHEAR-XY	PRINCIPAL STRESSES (ZERO SHEAR) ANGLE	MAJOR	MINOR	VON MISES
95515	CEN/4	-1.225000E-01	1.422333E+04	5.325159E+04	-1.245161E+02	-89.8172	5.325198E+04	1.422293E+04	4.775632E+04
		1.225000E-01	-1.679982E+03	-7.669265E+03	4.900249E+02	4.6466	-1.640154E+03	-7.709093E+03	7.033926E+03
	97855	-1.225000E-01	1.379127E+04	5.355337E+04	-1.245073E+02	-89.8206	5.355376E+04	1.379088E+04	4.816265E+04
		1.225000E-01	-1.934334E+03	-7.622219E+03	4.900392E+02	4.8883	-1.892424E+03	-7.664130E+03	6.914938E+03
	97854	-1.225000E-01	1.379127E+04	5.294980E+04	-1.244651E+02	-89.8179	5.295019E+04	1.379087E+04	4.757816E+04
		1.225000E-01	-1.934334E+03	-7.716312E+03	4.900458E+02	4.8103	-1.893095E+03	-7.757551E+03	7.005542E+03
	101152	-1.225000E-01	1.465543E+04	5.294973E+04	-1.245249E+02	-89.8137	5.295013E+04	1.465502E+04	4.735505E+04
		1.225000E-01	-1.425610E+03	-7.716322E+03	4.900106E+02	4.4274	-1.387670E+03	-7.754262E+03	7.161973E+03
	101151	-1.225000E-01	1.465543E+04	5.355344E+04	-1.245671E+02	-89.8165	5.355384E+04	1.465503E+04	4.793695E+04
		1.225000E-01	-1.425610E+03	-7.622209E+03	4.900040E+02	4.4935	-1.387101E+03	-7.660717E+03	7.069968E+03

Figure 45: Final NACA 0024 Tube Critical Stress f06

$$MS_{tube} = \frac{\sigma_{allowable}}{\sigma_{actual}} - 1 = \frac{95\ ksi}{1.5 * 53.6\ ksi} - 1 = 0.18$$

The fringe plot in Figure 46 shows that the maximum critical stress was on the inboard rib. It is a tensile stress on the lower half of the rib at the connecting section with the tube. This is the similar location as in the previous models. The stress has a magnitude of 42.6 ksi and occurs on node 97853 in element 92376 as seen in the f06 file in Figure 47. The corresponding MS is calculated below.

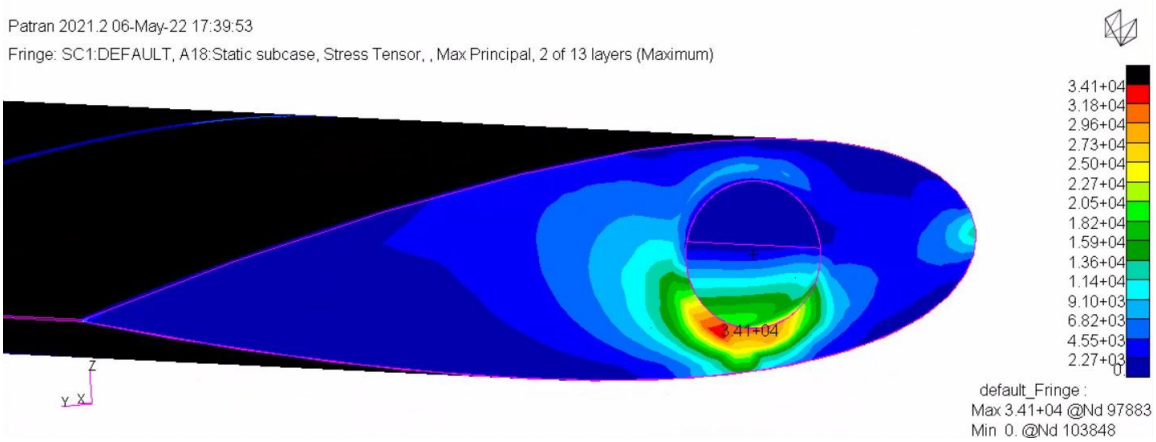

Figure 46: Final NACA 0024 Rib Critical Stress Fringe Plot

STRESSES IN QUADRILATERAL ELEMENTS (QUAD4) OPTION = BILIN

ELEMENT ID	GRID-ID	FIBER DISTANCE	STRESSES IN ELEMENT COORD SYSTEM NORMAL-X	NORMAL-Y	SHEAR-XY	PRINCIPAL STRESSES (ZERO SHEAR) ANGLE	MAJOR	MINOR	VON MISES
92376	CEN/4	-1.250000E-01	3.979595E+04	1.414261E+04	1.688726E+03	3.7501	3.990664E+04	1.403192E+04	3.506377E+04
		1.250000E-01	-3.501281E+04	-1.787631E+04	1.417707E+03	85.3025	-1.775982E+04	-3.512931E+04	3.042350E+04
	97853	-1.250000E-01	4.253710E+04	1.130016E+04	1.622242E+03	2.9649	4.262113E+04	1.121614E+04	3.826640E+04
		1.250000E-01	-3.626529E+04	-1.548805E+04	1.395267E+03	86.1753	-1.539477E+04	-3.635857E+04	3.161033E+04
	97883	-1.250000E-01	4.191181E+04	1.677785E+04	1.403285E+03	3.1858	4.198992E+04	1.669975E+04	3.661712E+04
		1.250000E-01	-3.598393E+04	-2.008056E+04	1.596942E+03	84.3222	-1.992179E+04	-3.614271E+04	3.135515E+04
	97882	-1.250000E-01	3.775101E+04	1.655974E+04	1.723945E+03	4.6206	3.789034E+04	1.642041E+04	3.291098E+04
		1.250000E-01	-3.407871E+04	-1.990660E+04	1.446520E+03	84.2312	-1.976046E+04	-3.422484E+04	2.975764E+04
	97852	-1.250000E-01	3.710069E+04	1.146458E+04	2.019422E+03	4.4765	3.725879E+04	1.130648E+04	3.308758E+04
		1.250000E-01	-3.377637E+04	-1.563743E+04	1.217020E+03	86.1786	-1.555614E+04	-3.385766E+04	2.935371E+04

Figure 47: Final NACA 0024 Rib Critical Stress f06

$$MS_{rib} = \frac{\sigma_{allowable}}{1.5 * \sigma_{actual}} - 1 = \frac{95\ ksi}{1.5 * 42.6\ ksi} - 1 = 0.49$$

A buckling analysis was performed and it was found that the first buckling mode occurs at a load factor of 2.03 towards the outer rib as shown in Figure 48. After applying a 1.5 factor of safety, it has a margin of safety of 0.35. The corresponding MS is calculated below.

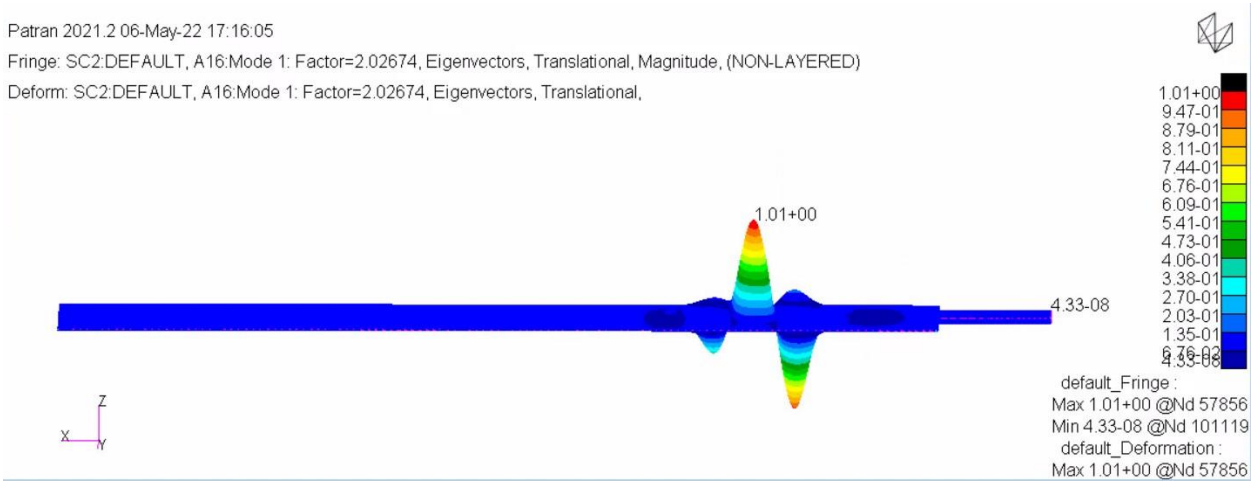

Figure 48: Final NACA 0024 Buckling Analysis (First Mode)

$$MS_{buckling} = \frac{2.03}{1.5} - 1 = 0.35$$

The critical margins of safety from the static and buckling FEA can be seen in Table 10. After comparing all MS values, the tube MS is the most critical. Based on the FEA, the analyzed CFRP antenna design appears to be structurally safe and reliable. This range of MS is appropriate for this preliminary antenna design. Further sizing would be expected during detailed design.

Table 10: Final NACA 0024 FEA Critical Margins of Safety

Tube Critical Margin of Safety	Ribs Critical Margin of Safety	Skin Critical Margin of Safety	Buckling Critical Margin of Safety
0.18	0.49	0.61	0.35

The first 5 natural frequencies of the final NACA 0024 are listed in Table 11 and their shapes are shown in Figure 49. The natural frequencies were taken from a modal FEA performed in Patran and Nastran. The final NACA 0024 antenna still has a large gap in frequencies around the 110 Hz blade passage frequency of the aircraft, meaning this preliminary design has a large buffer which is beneficial given that the boundary conditions have not been verified experimentally.

Table 11: Final NACA 0024 Natural Frequencies

Mode 1	14.36 Hz
Mode 2	47.98 Hz
Mode 3	79.59 Hz
Mode 4	142.64 Hz
Mode 5	177.47 Hz

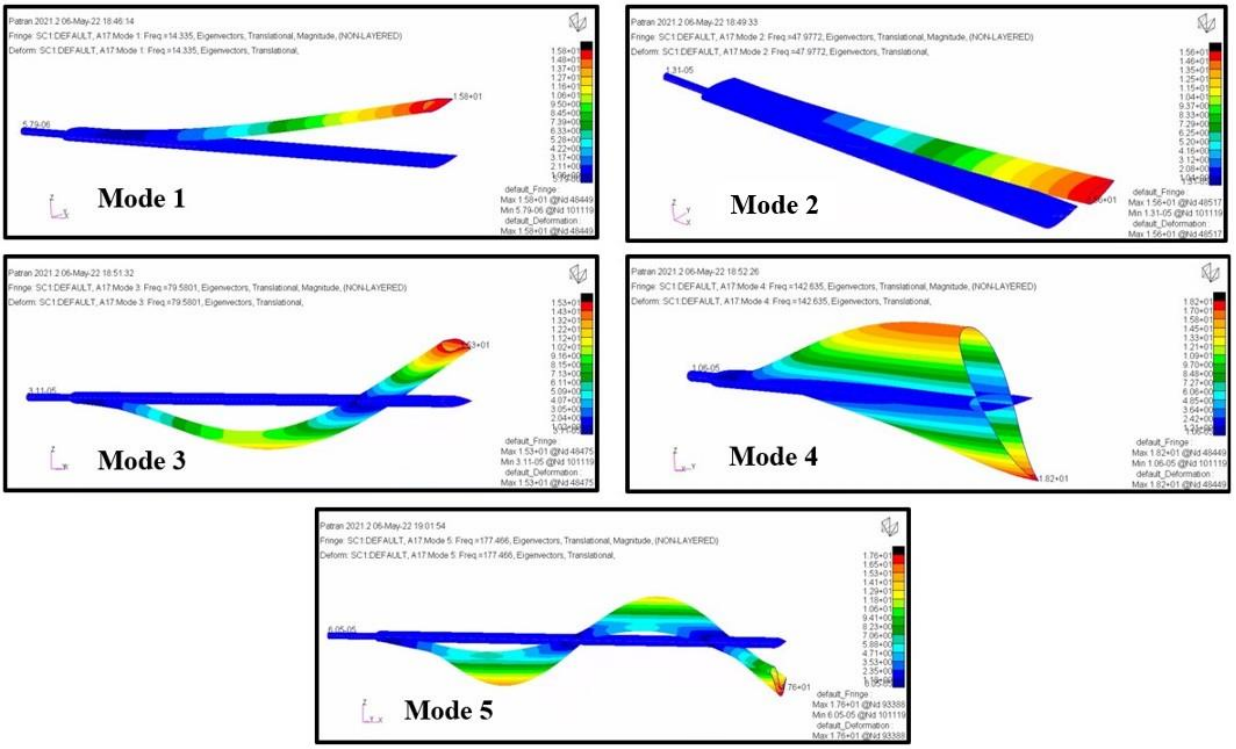

Figure 49: Final NACA 0024 Mode Shapes

The simulated analysis using a 5^{o} angle of attack showed that this analyzed 2x8 NACA 0024 antenna could withstand the aerodynamic loads experienced in flight and it has a significant

improvement in the electrical performance. The expected weight of this 2 in. x 8 in. NACA 0024 is 13.76 lbs. for one arm, but again, the vehicle is not weight critical. A proof-of-concept electrical prototype was constructed to physically test and verify the electrical performance.

5. Experimental Testing

5.1 Prototype Fabrication

An experimental prototype of the 2x8 NACA 0024 antenna was constructed to verify the electrical simulation data. Low-cost tooling was constructed using insulation foam commonly available at hardware stores and a hot wire technique. Given the size limitations for the manufacturing technique, the airfoil tool was only made 30 in. long, so that three separate sections had to be manufactured to construct a single side of the dipole. A laser cutter was used to fabricate two half airfoil section templates from 0.125 in. plywood that would be used as guides during the hotwire process. A top and bottom tool were constructed to make the top and bottom of the airfoil. Aluminum flashing was bonded onto the tool surface to give it a more continuous surface finish and help protect the tool when removing the cured part. In addition, a medium-density fiberboard backing was bonded to the back of the tool to help protect the tooling under pressure and extend its life. The surface was also covered with non-perforated release film to further protect the tool. The constructed airfoil tooling can be seen in Figure 51 and Figure 50. These figures of the tool were taken after 6 cure cycles which illustrates wear on the tool overtime.

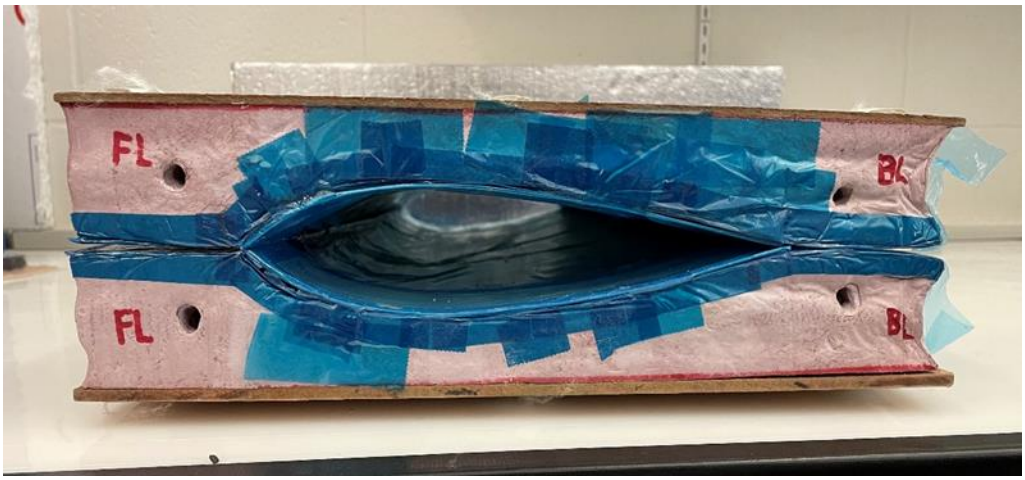

Figure 50: Airfoil Tool Top and Bottom Combined Shape

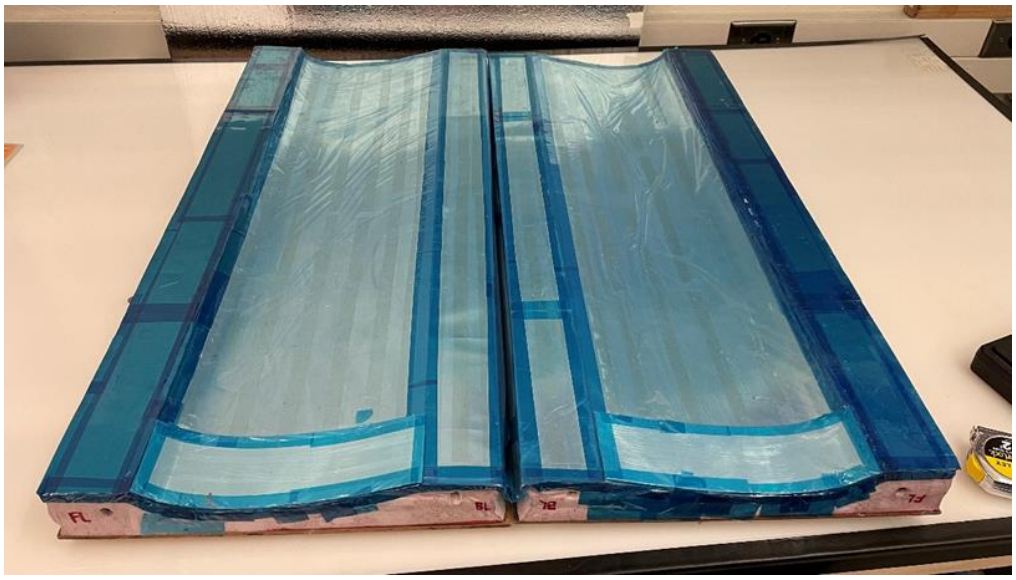

Figure 51: Airfoil Tool Surface

Three plies of AS4 bi-axial plain weave ($0^o/90^o$) fabric (3k, t=0.012 inches, CST-The Composite Store #CF 155-B, 5.7 oz/yd^2) and DPL 862 epoxy resin were laid on the top and bottom tool using a wet-layup technique and room temperature cure. These two halves were co-cured at the leading edge when placed together. An internal vacuum bag was placed between them to apply pressure and keep the airfoil shape, along with an external bag around the tool. Each part was left to cure for 24 hours under pressure. Since each antenna arm was made in three sections, the middle and outboard sections were slightly modified to include a joggle at one end to connect into the subsequent antenna section. Because this was an electrical prototype, each part was made using the minimum number of CFRP plies necessary (3 plies) for the entire antenna length. Given the insulative properties of the composite matrix, copper pieces were also placed at connection points between the individual sections and at rib locations to maintain an electrical connection when assembled. These thin copper strips were embedded in the laminate and co-cured. An additional 1 in. wide strip of CFRP cloth was used to partially sandwich the copper strips as this has been

shown to improve the electrical connection [2]. Release tape was applied to the exposed surface of the copper to prevent resin from flowing over the surface during the curing process. A single completed section can be seen in Figure 52. After curing, the antenna joggle slid into the antenna section where these copper pieces would touch on the outside of the joggle and the inside of the larger antenna piece as shown in Figure 53.

Figure 52: Single Antenna Section

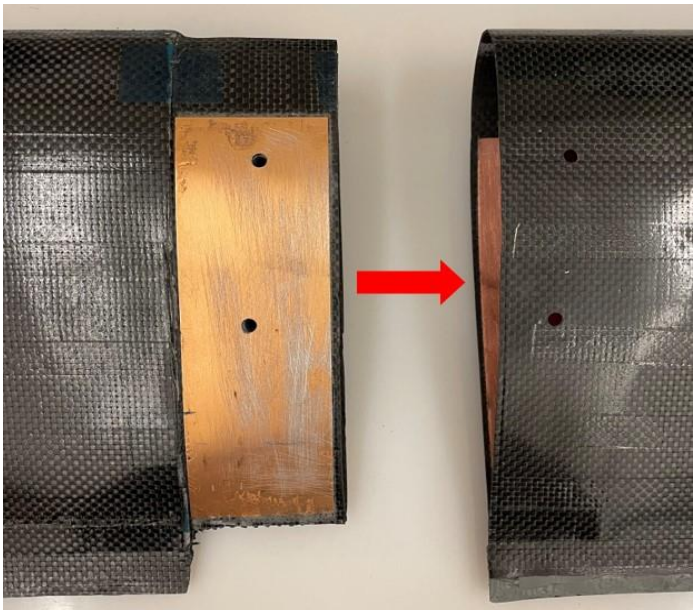

Figure 53: Antenna Section Connection

Ribs were machined from 6061-T6 aluminum that were 0.25 in. thick. The ribs were placed at the inboard locations. The trailing edges of each section and the ribs were bonded together using a Hysol adhesive at the same time after the initial curing process. During the bonding process, a steel tube was used to ensure proper placement of the ribs. The original tooling, sand bags, and clamps were used to ensure proper pressure was applied during the curing process. Holes were drilled at the connection points between the wing sections and nut plates were bonded on to allow for fasteners. While it is recognized that this approach will induce point loads into the anisotropic laminate, this approach was used for ease of manufacturing the electrical prototype. The 4130-steel tubes were slid into the two ribs on each antenna arm. For the electrical prototype, no fasteners were used to attach the tubes to the ribs. The rib and tube connection is shown in Figure 54.

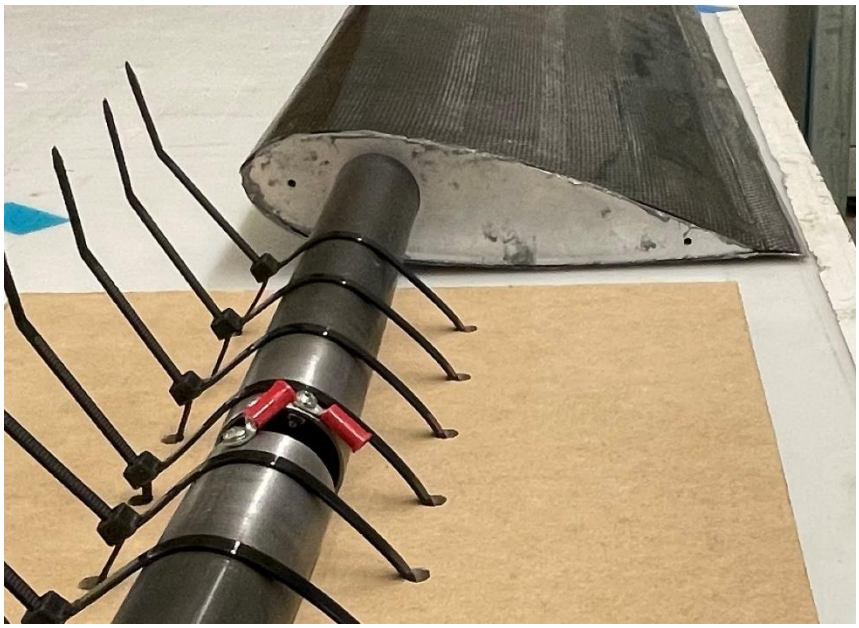

Figure 54: Rib and Tube Connection

The final structural design used 4130-steel for the tubes and ribs, but the physical prototype used 4130-steel for the tube and 6061-T6 aluminum for the ribs. The different materials could be

used in their place because they are not expected to cause any significant electrical differences in the testing and were more cost effective. The two antenna arms were held in place during testing with the steel tubes of each being zip tied onto a wooden board to prevent any stress on the antenna electrical connection during the installation and testing. The antenna was fed by splitting a piece of coax cable and fastening it to the end of each tube using eyelet connectors. The fully assembled prototype antenna can be seen in Figure 55.

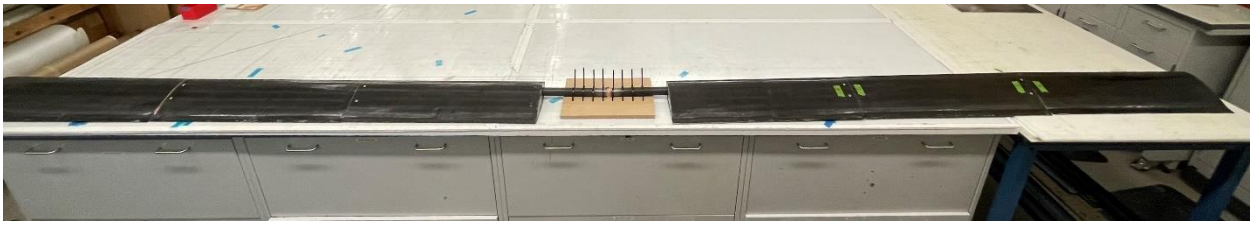

Figure 55: Full Prototype Antenna Assembly

While there were some deviations between the as-built prototype and the final simulated design, these modifications are not expected to significantly change the resonance of the antenna. The design of the prototype was driven by cost limitations, thus the minimum number of plies were used in the laminate and lower-accuracy manufacturing methods were used for the tooling development. While the prototype design was sufficient to verify antenna resonance, it was not suitable for any structural or modal testing. A future prototype for structural testing should use higher fidelity tools and materials to ensure maximum performance in all aspects.

5.2 Experimental Results

Measurements for the experimental prototype antenna were taken in an anechoic chamber. The experimental setup is shown in Figure 56. The S_{11} of the antennas was measured by connecting

a 50-ohm cable to the coax connector attached to the antenna. Prior to the measurement, a calibration was performed to eliminate the cable responses.

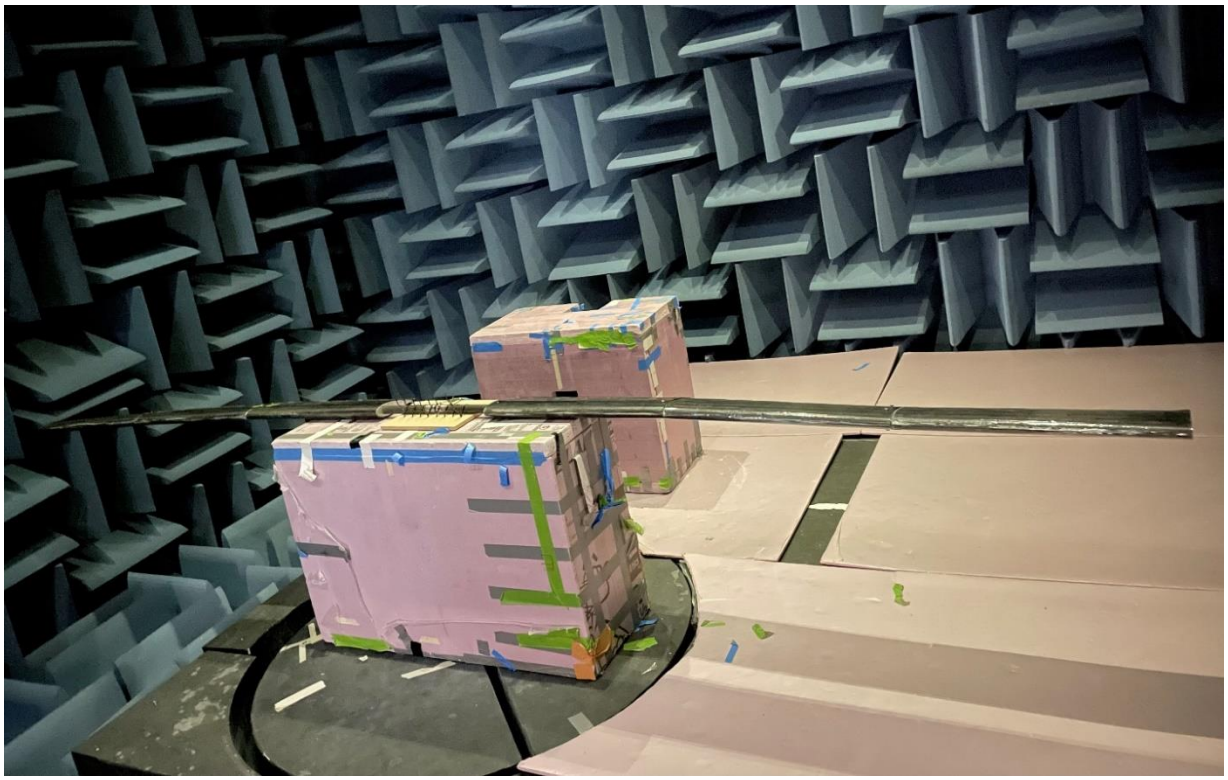

Figure 56: Experimental Testing Setup

Figure 57 shows a comparison of the experimental S_{11} measured within the anechoic chamber of the prototype NACA 0024 antenna and the original tube antenna (tube measurements were conducted in September 2016 in the same chamber), along with the simulated S_{11} of the NACA airfoil and the tube.

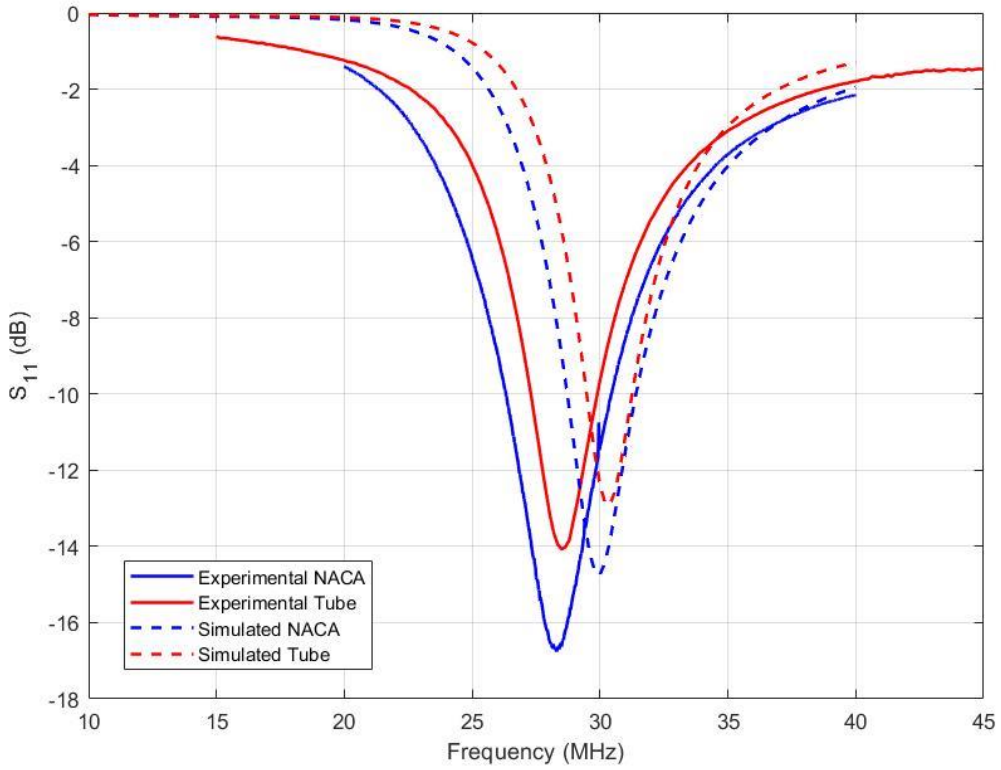

Figure 57: Experimental and Simulated S_{11} Comparison

The experimental measurements show that the prototype NACA antenna had a resonant frequency of 28.3 MHz and a 10-dB impedance bandwidth of 4.2 MHz (26.3 MHz – 30.5 MHz) compared to the as-measured tube antenna which had a resonant frequency of 28.5 MHz and a bandwidth of 2.5 MHz (27.3 MHz – 29.8 MHz). This is a 1.7 times improvement in bandwidth. Each experimentally measured antenna had about 1.6 times larger bandwidth than their simulated counterpart. This is attributed to the fact that a portion of the Twin Otter aircraft was included in the simulations whereas the physical measurements only included the antennas. It is also attributed to the geometric abstraction used in feeding the antenna. Both experimental results had a downward shift in resonance by an average of 1.8 MHz and in general the differences between the simulated and measured S_{11} are about the same for the two designs. The data shows that the newly

designed antenna has improved bandwidth when directly compared to the original tube in similar conditions. The agreement between the simulations and measured S_{11} provides confidence that the design will improve electrical performance and it would be expected that if the NACA antenna were installed on the tail of the Twin Otter, that it would exhibit similar bandwidth improvement compared to the installed tube antenna in Figure 3.

6. Conclusions and Future Recommendations

6.1 Conclusions

A larger CFRP antenna design for replacement of the steel tube dipole antenna on the Twin Otter has been investigated and improved bandwidth is expected. To determine the ideal new design, structural sizing of antenna candidates was performed. The original antenna had minimal drag and range reduction because of its small diameter, but its small size limited its electrical bandwidth. Given that these metrics oppose the larger antenna requirement, the ideal candidate design had to exhibit satisfactory performance for all three characteristics (electrical performance, impact on vehicle range, and structural stability). From the initial comprehensive trade study, two candidate designs were identified that performed best overall for the analyzed characteristics. These were a 2 in. x 8 in. NACA 0024 cross-sectional antenna and a 3 in. x 9 in. elliptical cross-sectional antenna. Based on further analysis using finite element analysis, the 2x8 NACA 0024 antenna was selected as the final candidate design, further analyzed, and electrically tested. The conclusions of this work include:

1) By replacing the original steel design with a CFRP design, a larger antenna could be supported, resulting in a wider operational bandwidth. In addition, it is expected that the vehicle range will be maintained by using an aerodynamic shape/airfoil for this larger design.
2) The 2x8 NACA 0024 antenna is expected to improve the vehicle range by 5% compared to the original tube antenna because of its more aerodynamic shape.
3) The NACA antenna had around 1.75 times improvement in simulated bandwidth compared to the original tube. A proof-of-concept prototype was manufactured for experimental electrical testing. Electrical testing of the prototype antenna within the anechoic chamber

verified that the new NACA antenna works as designed and has a 1.7 times improvement in bandwidth compared to the original tube antenna under similar conditions. The experimental bandwidth improvement is very similar to the simulated bandwidth improvement. It would be expected that if the NACA antenna were installed on the tail of the Twin Otter, that it would exhibit similar bandwidth improvement compared to the installed tube antenna.

From this study, it can be concluded that the new 2 in. x 8 in. NACA 0024 antenna design has the potential to improve mission capabilities with an improved bandwidth and improved vehicle range. Though the improvement in bandwidth can only conclusively be determined for a fully installed antenna with a matching network, in all instances of comparison between the NACA airfoil antenna and the original tube antenna, bandwidth improvements were observed. Thus, there is high confidence that improved bandwidth can be achieved.

6.2 Future Recommendations

A thorough investigation was performed to develop a potentially improved bandwidth antenna design for the Twin Otter. However, detailed design is required for this design concept to further asses the performance implications of this larger antenna design. Some recommendations for future improvement include:

1) A higher fidelity prototype should be manufactured to physically assess structural and modal characteristics. An experimental analysis of these characteristics is important to verify the simulation data, in particular the applied boundary conditions, and confirm that the structure will respond appropriately to the imposed conditions.

2) A future analysis should be more conservative with the boundary conditions. The top nodes of the rib and skin connection were fixed in the x-direction to simulate the antenna bearing against the aircraft. Upon reflection, this constraint gives a load path which understates the potential of the load having to get from the skins to the ribs and tube. The more conservative approach would be to remove this bearing path and ensure that the rest of the structure can support the load. If the load becomes significantly larger, the material for the tube and rib can still be swapped for a higher strength material like the 52100-steel.
3) A more detailed design assessment should be performed to produce a more practically manufacturable design and improve maintenance and assembly capabilities. The rib design will need to be adjusted since there is no real way to connect and fasten the spar tube for the current configuration. A more robust feeding technique will be needed to ensure a strong connection during flight. The current design is spliced at the center, thus there is no load path. The original tube antenna used a fiberglass tube to connect the two sides of the center pieces and a similar design is recommended to use in the new NACA antenna's final design. The use of fasteners through the composite must be further assessed to ensure airworthiness. Finally, a buffer should be included in the final design like the original tube antenna had with the polycarbonate cuffs. This will help prevent chattering of the antenna against the aircraft.
4) A computational fluid dynamics (CFD) analysis should be conducted in the future to determine the aerodynamic pressures imposed on the antenna. This could be used to more accurately assess the stresses acting on the antenna. This CFD analysis could also be used for a stability and control analysis. The stability and control derivatives of the aircraft

would need to be assessed to ensure that adding a lifting body so far aft of the aircraft would not affect its overall stability.

5) Gust loads and flutter were not considered in this analysis. These should be considered in a future analysis. Gust could instantly cause a higher load on the structure, so it would need to be verified that the antenna could withstand an instantaneous load increase caused by this. Also, a CFD analysis and a physical vibration test could help determine the structure's stability under the impact of flutter.
6) Future electrical testing within the anechoic chamber could include an assembled Twin Otter tail structure with the prototype antenna to evaluate it with potential aircraft integration effects. When the NACA antenna and the tube antenna were directly compared in similar conditions, the data shows that the NACA antenna has improved bandwidth. The tube antenna bandwidth has been measured while installed on the Twin Otter in the field and with a tail section in the anechoic chamber. The NACA antenna is expected to improve bandwidth if installed on the Twin Otter, but a physical test that includes the tail section would confirm this conclusion.

References

[1] Arnold, E. J., Rodriguez-Morales, F., Paden, J., Leuschen, C., Keshmiri, S., Yan, S., Ewing, M., Hale, R., Mahmood, A., Blevins, A., Mishra, A., Karidi, T., Miller, B., and Sonntag, J., "HF/VHF Radar Sounding of Ice from Manned and Unmanned Airborne Platforms," *Geosciences*, Vol. 8, No. 5, May 2018.

[2] Patil, A. S., and Arnold, E. J., "Characterizing Carbon Fiber Conductivity for Structural Antenna Applications," *IEEE Trans. on Antennas and Propag., IEEE Transactions on Antennas and Propagation*, Aug. 2021. DOI: 10.1109/TAP.2021.3102037.

[3] Hoerner, S. F., Fluid-Dynamic Drag, Published by Author, 1958.

[4] HFSS, High Frequency Structure Simulator, Software Package, Ansys, Canonsburg, PA, 2021

[5] NX, Software Package, ver. 1915, Siemens, 2020.

[6] *Military Handbook - MIL-HDBK-5H: Metallic Materials and Elements for Aerospace Vehicle Structures (Knovel Interactive Edition)*. (2003). Norwich: Knovel Corporation.

[7] Clarkson, E. (2019). *Solvay (Formerly ACG) MTM45- 1/CF0525-36%RW 3K PW AS4 Fabric Qualification Statistical Analysis Report. Wichita State University*. https://www.wichita.edu/industry_and_defense/NIAR/Research/cytec-mtm45-1/NCP-RP-2009-037NCACG3KPWAS4FabricStatAnalysisReport01-08-19.pdf

[8] Cengel, Y. A., and Cimbala, J. M., *Fluid Mechanics Fundamentals and Applications*, 4th ed., McGraw Hill Education, New York, 2017.

[9] Airfoil Tools. (n.d.). Retrieved from http://airfoiltools.com/index.

[10] Budynas, R. G., and Nisbett, J. K., *Shigley's Mechanical Engineering Design*, 10th ed., McGraw-Hill Education, New York, 2014.

[11] Patran, Software Package, ver. 2021.2, MSC Software, Irvine, CA, 2021.

[12] Nastran, Software Package, ver. 2021.2, MSC Software, Irvine, CA, 2021.

[13] Inman, D. J., *Engineering Vibration*, 4th ed., Pearson Education, Boston, 2014.

[14] Genesys, Software Package, Software Package, ver. 2015.08, Keysight Technologies, 2015.

[15] Rios, A., and Arnold, E. J. "Improved Carbon Fiber Reinforced Plastic Structural Antenna Design for near-HF Remote Sensing Applications," *AIAA 2022-2554. AIAA SciTech 2022 Forum*. January 2022. https://doi.org/10.2514/6.2022-2554

Appendix

A1. Initial Trade Study Calculations

The stress and margin of safety calculations used in the initial trade study for the larger planform designs can be seen below (with some values being rounded off):

For 2x4 ellipse:

$$L = \frac{1}{2}\rho V^2 c_l S = \frac{1}{2} * 0.07654 \frac{lb_m}{ft^3} * \left(287 \frac{ft}{s}\right)^2 * 0.3 * 2.406 ft^2 * \left(\frac{1\ lb_f}{32.2\ lb_m * \frac{ft}{s^2}}\right) = 70.9\ lbs$$

$$M = L * l = 70.9\ lb * 86.6\ in = 6142\ lb * in$$

$$\sigma_{tube} = \frac{Mr}{I} = \frac{(6142\ lb * in) * \frac{1.207}{2} in}{0.0912\ in^4} = 40.638\ ksi$$

$$MS_{tube} = \frac{\sigma_{allowable}}{1.5 * \sigma_{actual}} - 1 = \frac{147\ ksi}{1.5 * 40.638\ ksi} - 1 = 1.41$$

$$\sigma_{skin} = \frac{Mr}{I} = \frac{(6142\ lb * in) * \frac{2}{2} in}{0.3877\ in^4} = 15.844\ ksi$$

$$MS_{skin} = \frac{\sigma_{allowable}}{1.5 * \sigma_{actual}} - 1 = \frac{38\ ksi}{1.5 * 15.844\ ksi} - 1 = 0.6$$

For 3x9 ellipse:

$$L = \frac{1}{2}\rho V^2 c_l S = \frac{1}{2} * 0.07654 \frac{lb_m}{ft^3} * \left(287 \frac{ft}{s}\right)^2 * 0.26 * 5.231 ft^2 * \left(\frac{1\ lb_f}{32.2\ lb_m * \frac{ft}{s^2}}\right) = 132.2\ lbs$$

$$M = L * l = 132.2\ lb * 83.7\ in = 11065\ lb * in$$

$$\sigma_{tube} = \frac{Mr}{I} = \frac{(11065\ lb * in) * \frac{1.207}{2} in}{0.0912\ in^4} = 73.207\ ksi$$

$$MS_{tube} = \frac{\sigma_{allowable}}{1.5 * \sigma_{actual}} - 1 = \frac{147\ ksi}{1.5 * 73.207\ ksi} - 1 = 0.28$$

$$\sigma_{skin} = \frac{Mr}{I} = \frac{(11065\ lb * in) * \frac{2}{2} in}{1.942\ in^4} = 8.547\ ksi$$

$$MS_{skin} = \frac{\sigma_{allowable}}{1.5 * \sigma_{actual}} - 1 = \frac{38\ ksi}{1.5 * 8.547\ ksi} - 1 = 1.96$$

For 2x8 NACA 0024:

$$L = \frac{1}{2}\rho V^2 c_l S = \frac{1}{2} * 0.07654 \frac{lb_m}{ft^3} * \left(287 \frac{ft}{s}\right)^2 * 0.31 * 4.545 ft^2 * \left(\frac{1\ lb_f}{32.2\ lb_m * \frac{ft}{s^2}}\right) = 137.93\ lbs$$

$$M = L * l = 137.9\ lb * 81.3\ in = 11213\ lb * in$$

$$\sigma_{tube} = \frac{Mr}{I} = \frac{(11213\ lb * in) * \frac{1.207}{2} in}{0.0912\ in^4} = 74.194\ ksi$$

$$MS_{tube} = \frac{\sigma_{allowable}}{1.5 * \sigma_{actual}} - 1 = \frac{147\ ksi}{1.5 * 74.194\ ksi} - 1 = 0.32$$

$$\sigma_{skin} = \frac{Mr}{I} = \frac{(11213\ lb * in) * \frac{2}{2} in}{0.7315\ in^4} = 15.328\ ksi$$

$$MS_{skin} = \frac{\sigma_{allowable}}{1.5 * \sigma_{actual}} - 1 = \frac{38\ ksi}{1.5 * 15.328\ ksi} - 1 = 0.65$$

For 3x12.5 NACA 0024:

$$L = \frac{1}{2}\rho V^2 c_l S = \frac{1}{2} * 0.07654 \frac{lb_m}{ft^3} * \left(287 \frac{ft}{s}\right)^2 * 0.31 * 6.997 ft^2 * \left(\frac{1\ lb_f}{32.2\ lb_m * \frac{ft}{s^2}}\right) = 212.32\ lbs$$

$$M = L * l = 212.32\ lb * 80.6\ in = 17113\ lb * in$$

$$\sigma_{tube} = \frac{Mr}{I} = \frac{(17113\ lb * in) * \frac{1.207}{2} in}{0.0912\ in^4} = 113.233\ ksi$$

$$MS_{tube} = \frac{\sigma_{allowable}}{1.5 * \sigma_{actual}} - 1 = \frac{147\ ksi}{1.5 * 113.233\ ksi} - 1 = -0.13$$

$$\sigma_{skin} = \frac{Mr}{I} = \frac{(17113\ lb * in) * \frac{2}{2} in}{2.629\ in^4} = 9.766\ ksi$$

$$MS_{skin} = \frac{\sigma_{allowable}}{1.5 * \sigma_{actual}} - 1 = \frac{38\ ksi}{1.5 * 9.766\ ksi} - 1 = 1.6$$

For 2x5.6 Eppler 863:

$$L = \frac{1}{2}\rho V^2 c_l S = \frac{1}{2} * 0.07654 \frac{lb_m}{ft^3} * \left(287 \frac{ft}{s}\right)^2 * 0.45 * 3.29 ft^2 * \left(\frac{1\ lb_f}{32.2\ lb_m * \frac{ft}{s^2}}\right) = 144.93\ lbs$$

$$M = L * l = 144.93\ lb * 84.6\ in = 12261\ lb * in$$

$$\sigma_{tube} = \frac{Mr}{I} = \frac{(12261\ lb * in) * \frac{1.207}{2} in}{0.0912\ in^4} = 81.129\ ksi$$

$$MS_{tube} = \frac{\sigma_{allowable}}{1.5 * \sigma_{actual}} - 1 = \frac{147\ ksi}{1.5 * 81.129\ ksi} - 1 = 0.21$$

$$\sigma_{skin} = \frac{Mr}{I} = \frac{(12261\ lb * in) * \frac{2}{2} in}{0.5235\ in^4} = 23.421\ ksi$$

$$MS_{skin} = \frac{\sigma_{allowable}}{1.5 * \sigma_{actual}} - 1 = \frac{38\ ksi}{1.5 * 23.421\ ksi} - 1 = 0.08$$

For 3x8.4 Eppler 863:

$$L = \frac{1}{2}\rho V^2 c_l S = \frac{1}{2} * 0.07654 \frac{lb_m}{ft^3} * \left(287 \frac{ft}{s}\right)^2 * 0.45 * 4.88 ft^2 * \left(\frac{1\ lb_f}{32.2\ lb_m * \frac{ft}{s^2}}\right) = 215.09\ lbs$$

$$M = L * l = 215.09\ lb * 83.7\ in = 18003\ lb * in$$

$$\sigma_{tube} = \frac{Mr}{I} = \frac{(18003\ lb * in) * \frac{1.207}{2} in}{0.0912\ in^4} = 119.118\ ksi$$

$$MS_{tube} = \frac{\sigma_{allowable}}{1.5 * \sigma_{actual}} - 1 = \frac{147\ ksi}{1.5 * 119.118\ ksi} - 1 = -0.18$$

$$\sigma_{skin} = \frac{Mr}{I} = \frac{(18003\ lb * in) * \frac{2}{2} in}{1.824\ in^4} = 14.804\ ksi$$

$$MS_{skin} = \frac{\sigma_{allowable}}{1.5 * \sigma_{actual}} - 1 = \frac{38\ ksi}{1.5 * 14.804\ ksi} - 1 = 0.71$$

A2. Final Lift Load Comparison Calculations

The lift load calculations used in Table 8 can be seen below (with some values being rounded off):

For 3° angle of attack and V_{ne}:

$$L = \frac{1}{2}\rho V^2 c_l S = \frac{1}{2} * 0.07654 \frac{lb_m}{ft^3} * \left(287 \frac{ft}{s}\right)^2 * 0.31 * 4.545 ft^2 * \left(\frac{1\ lb_f}{32.2\ lb_m * \frac{ft}{s^2}}\right) = 138\ lbs$$

For 5° angle of attack and V_{ne}:

$$L = \frac{1}{2}\rho V^2 c_l S = \frac{1}{2} * 0.07654 \frac{lb_m}{ft^3} * \left(287 \frac{ft}{s}\right)^2 * 0.5 * 4.545 ft^2 * \left(\frac{1\ lb_f}{32.2\ lb_m * \frac{ft}{s^2}}\right) = 221\ lbs$$

For 15° angle of attack and V_{mc}:

$$L = \frac{1}{2}\rho V^2 c_l S = \frac{1}{2} * 0.07654 \frac{lb_m}{ft^3} * \left(111 \frac{ft}{s}\right)^2 * 1.25 * 4.545 ft^2 * \left(\frac{1\ lb_f}{32.2\ lb_m * \frac{ft}{s^2}}\right) = 83\ lbs$$

For 10° angle of attack and V=190ft/s:

$$L = \frac{1}{2}\rho V^2 c_l S = \frac{1}{2} * 0.07654 \frac{lb_m}{ft^3} * \left(190 \frac{ft}{s}\right)^2 * 0.95 * 4.545 ft^2 * \left(\frac{1\ lb_f}{32.2\ lb_m * \frac{ft}{s^2}}\right) = 185\ lbs$$

For 15° angle of attack and 1.2*V_{mc}:

$$L = \frac{1}{2}\rho V^2 c_l S = \frac{1}{2} * 0.07654 \frac{lb_m}{ft^3} * \left(133 \frac{ft}{s}\right)^2 * 1.25 * 4.545 ft^2 * \left(\frac{1\ lb_f}{32.2\ lb_m * \frac{ft}{s^2}}\right) = 119\ lbs$$